Contents lists available at ScienceDirect

Antiviral Research

journal homepage: www.elsevier.com/locate/antiviral

Short communication

Inhibition of porcine endogenous retrovirus (PERV) replication by HIV-1 gene expression inhibitors

Minyi Shi [a,b,1], Xin Wang [b,2], Mika Okamoto [b], Sonshin Takao [a], Masanori Baba [b,*]

[a] Frontier Science Research Center, Kagoshima University, Kagoshima 890-8544, Japan
[b] Division of Antiviral Chemotherapy, Center for Chronic Viral Diseases, Graduate School of Medical and Dental Sciences, Kagoshima University, Kagoshima 890-8544, Japan

ARTICLE INFO

ABSTRACT

Porcine endogenous retrovirus (PERV) is persistently integrated into the host genomic DNA as a provirus and released from a variety of porcine cells. PERV infects a certain range of human cells, which is a major concern in xenotransplantation. Therefore, the use of viral gene expression inhibitors could be envisaged, if they reduce PERV production from porcine organs and minimize viral transmission to human recipients. In the present study, four HIV-1 gene expression inhibitors were examined for their inhibitory effect on PERV replication in porcine cells constitutively producing the virus. Among the compounds, the fluoroquinolone derivative K-37 and the bacterial product EM2487 displayed potent and selective inhibition of PERV replication in the cells mediated by the suppression of viral mRNA synthesis. Thus, retroviral gene expression inhibitors may be able to reduce the risk of PERV transmission.

© 2009 Elsevier B.V. All rights reserved.

Xenotransplantation, the grafting of cells, tissues, or organs into different species, is a possible solution to overcome the extreme shortage of human allografts for transplantation (Cooper and Keogh, 2001). Among the animals, non-human primates and pigs are considered to be suitable donors for xenotransplantation. The use of non-human primates as organ donors is associated with a high risk of transmitting various infectious pathogens to humans (Allan, 2003). Apart from immunological rejection, pigs may be more suitable donors than non-human primates because of the resemblance of their organ sizes and a lower risk of transmitting various infectious pathogens. However, porcine endogenous retrovirus (PERV) is still a major obstacle to successful xenotransplantation with sufficient safety. PERV is a type C retrovirus persistently integrated into the host genomic DNA as a provirus. Multiple copies of PERV proviral DNA exist in all of the breeds examined to date (Louz et al., 2008). PERV is classified into three subtypes, such as PERV-A, -B, and -C, based on the divergence of its envelope genes.

It has been demonstrated that PERV particles are released from a variety of porcine cells and infect a certain range of human cells (Martin et al., 1998; Patience et al., 1997; Wilson et al., 1998). There

are a number of patients who received porcine tissues, such as pancreatic islet cells, skin, liver, and kidney; nevertheless PERV infection has not been observed in these individuals (Heneine et al., 1998; Paradis et al., 1999; Patience et al., 1998). However, long-lived microchimerism was found in some patients treated by extracorporeal splenic perfusion, which might increase a potential risk of PERV infection through the activation of viral replication (Paradis et al., 1999). An immunosuppressive treatment upon organ transplantation may also increase a risk of PERV transmission. The use of antiretrovirals would be the first option to minimize the possibility of PERV transmission to recipients, if they could have an inhibitory effect on PERV replication without serious side effects. Among the antiretrovirals, zidovudine (AZT) and didanosine (ddI) proved to be active against PERV replication in cell cultures (Powell et al., 2000; Qari et al., 2001). We have previously demonstrated that the acyclic nucleoside phosphonate tenofovir (PMPA), an HIV-1 reverse transcriptase (RT) inhibitor, selectively inhibits PERV replication in human cells (Shi et al., 2007). However, such RT inhibitors cannot suppress the production of PERV from the porcine cells in which its proviral DNA is integrated. Therefore, it would be very useful if an inhibitor of PERV gene expression could be identified. In the present study, we have examined four inhibitors of HIV-1 gene expression for their antiviral activity against PERV replication in porcine cells persistently infected with the virus and found that the fluoroquinolone derivative K-37 (Baba et al., 1998) and the bacterial product EM2487 (Baba et al., 1999) are potent and selective inhibitors of PERV replication.

K-37 and the nuclear factor κB (NF-κB) inhibitor cepharanthine (Okamoto et al., 1998) were provided by Daiichi Pharmaceutical
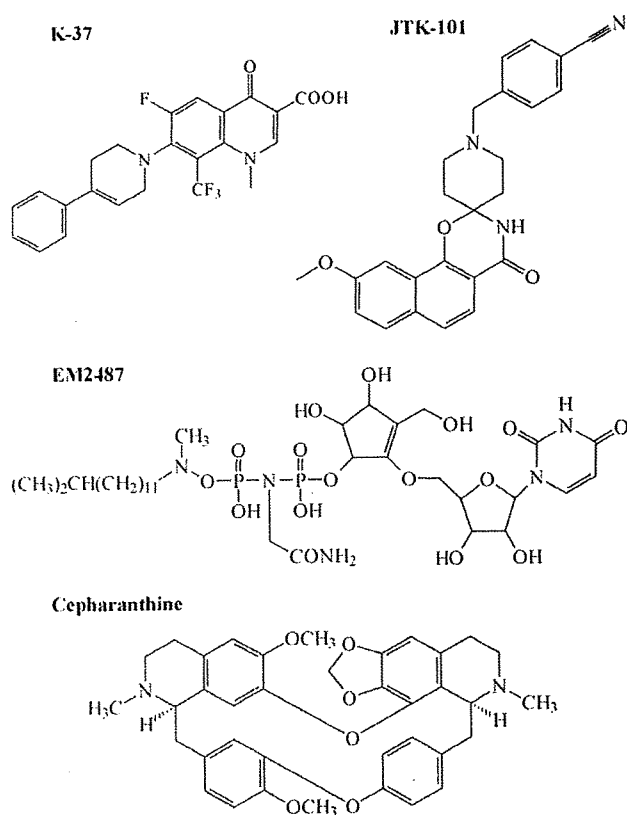
Fig. 1. Chemical structures of test compounds.

Co. (Tokyo, Japan) and Kaken Shoyaku (Mitaka, Japan), respectively. JTK-101 (Wang et al., 2007) was synthesized by Japan Tobacco Co. (Takatsuki, Japan). EM2487 was provided by Esai Co. (Tsukuba, Japan). These compounds (Fig. 1) were chosen for this study, because their antiviral activity against HIV-1 replication in chronically infected cells had been demonstrated (Baba et al., 1998, 1999; Okamoto et al., 1998; Wang et al., 2007). All compounds were dissolved in dimethyl sulfoxide (DMSO) at 10 mM or higher concentrations to exclude any antiviral or cytotoxic effect of DMSO and stored −20 °C until use. The porcine embryonic kidney cell line PK15, which produces PERV particles, was obtained from the American Type Culture Collection. The cells were maintained in Eagle's minimal essential medium supplemented with 10% fetal bovine serum, 0.1 mM nonessential amino acids, 1 mM sodium pyruvate, 1.5 g/l sodium bicarbonate, and antibiotics.

The activity of the compounds against persistent PERV infection was based on the inhibition of PERV particle production from PK15 cells. PK15 cells were seeded in a 24-well plate (2.5×10^4 cells/well). After incubation for 16 h at 37 °C, the culture supernatants were removed and the cell monolayer was washed by phosphate-buffered saline (PBS), and then 2 ml of fresh medium containing various concentrations of the test compounds was added to each well. After a 48-h incubation period, the culture supernatants were collected and filtered (0.45 μm pore size). Then the filtrates were mixed with 22% (w/v) polyethylene glycol 6000 solution. After incubation for 5 h at 4 °C with continuous stirring, the mixture was centrifuged at 15,000 rpm for 15 min at 4 °C. The pellets contained PERV particles released from PK15 cells. The inhibition of PERV particle production was determined by the decrease of PERV reverse transcriptase activity using a commercial RT assay kit (Roche, Mannheim, Germany). The pellets obtained above were resuspended in lysis buffer supplied by the assay kit and subjected to reverse transcription reaction for 2 h, according to the Manufac-

turer's instructions, except that $MgCl_2$ in the reaction mixture was replaced by $MnCl_2$ (Phan-Thanh et al., 1992). All experiments were carried out in duplicate.

The antiviral activity of test compounds was also determined by the inhibition of PERV mRNA expression in PK15 cells. PK15 cells were seeded and cultured in the medium containing test compounds in the same manner as described for the antiviral assay. After a 48-h incubation, the culture supernatants were removed, and the cells were extensively washed with PBS, trypsinized, and washed again with PBS. Total RNA was extracted from the cells with RNeasy Mini Kit (Qiagen) and subjected to real-time RT-PCR analysis. The PERV mRNA level was determined using the sense primer (5′-AGCTCCGGGAGGCCTACTC-3′), the antisense primer (5′-ACAGCCGTTGGTGTGGTCA-3′), and the Taqman® probe (5′-FAM-CCACCGTGCAGGAAACCTCGAGACT-TAMRA-3′). The primer pair amplifies a region of the pol gene of PERV (Paradis et al., 1999). The nucleotide sequences used for the construction of the primers and probe were based on the reports by B. Bartosch, R.A. Weiss and Y. Takeuchi (GeneBank accession numbers: AY099323 and AY099324). The final concentrations of the primer pairs and probe were 200 and 100 nM, respectively. The Taqman® PCR reagent kit and Taqman® Multiscribe™ reverse transcription reagent kit (Applied Biosystems, Roche, Branchburg, NJ) were used according to the Manufacturer's instructions. Each sample was run in triplicate. Nonspecific inhibition of host cellular mRNA synthesis by the test compounds was determined with the Taqman 18S rRNA reagent kit (Applied Biosystems).

Cytotoxicity of the test compounds was determined by a tetrazolium dye method (Tetracolor One®, Seikagaku Corporation, Tokyo, Japan) (Yamamoto et al., 2001). PK15 cells were seeded and cultured in the medium containing test compounds in the same manner, as described in the antiviral assay. After a 48-h incubation, 1.5 ml of the culture supernatants were removed and 25 μl of the dye was added to each well. After a 4-h incubation at 37 °C, the specific (450 nm) and reference (630 nm) absorbances were monitored for each well by a microplate reader.

When four HIV-1 gene expression inhibitors were examined for their inhibitory effect on PERV replication in PK15 cells, K-37 and EM2487 displayed dose-dependent reduction of PERV RT activity in culture supernatants (Fig. 2A and C). K-37 and EM2487 did not show a direct inhibitory effect on PERV RT activity (data not shown). These compounds did not display apparent cytotoxicity to PK15 cells at concentrations up to 1 and 10 μM, respectively, indicating that K-37 and EM2487 are selective inhibitors of PERV replication in porcine cells. In contrast, JTK-101 and cepharanthine did not show any activity against PERV replication at the highest concentration tested (1 μM) (Fig. 2B and D). Since PERV proviral DNA is integrated in the genome of the host cells, the compounds were also examined for their inhibitory effect on viral mRNA synthesis in PK15 cells. As shown in Fig. 3, dose-dependent suppression of PERV mRNA synthesis was observed for K-37 and EM2487 but not for JTK-101 or cepharanthine. These results are in accordance with those obtained in the RT assay (Fig. 2). The 50% effective concentration (EC_{50}) of K-37 for PERV replication and its 50% inhibitory concentration (IC_{50}) for viral mRNA synthesis were 0.35 ± 0.04 and 0.34 ± 0.05 μM, respectively (Table 1). On the other hand, its 50% cytotoxic concentration (CC_{50}) was 4.63 ± 1.62 μM, suggesting that K-37 is a selective inhibitor of PERV gene expression. Similarly, the EC_{50}, IC_{50}, and CC_{50} of EM2487 were 5.44 ± 1.40, 4.36 ± 0.30, and >10 μM, respectively.

K-37 is a potent and selective inhibitor of HIV-1 replication in both acutely and chronically infected cells at submicromolar concentrations (Baba et al., 1998). K-37 could inhibit Tat-dependent transactivation, yet it was not an inhibitor of Tat itself or its cofactor CDK9/cyclin T1. Since PERV does not generate Tat protein, it is apparent that the anti-PERV activity of K-37 is not due to the inhi-
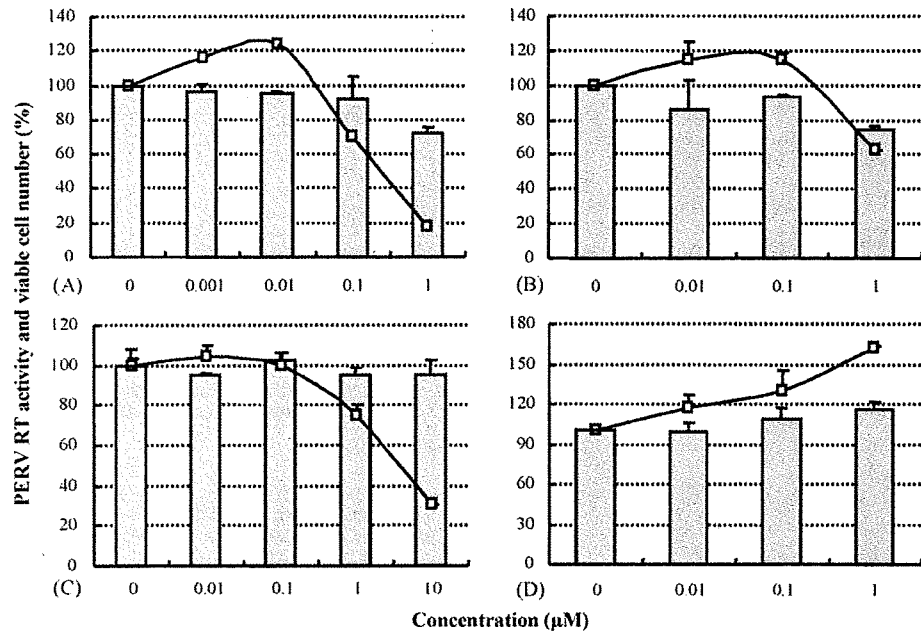
Fig. 2. Inhibitory effects of the test compounds on PERV replication in PK15 cells. PK15 cells were cultured in the presence of various concentrations of (A) K-37, (B) JTK-101, (C) EM2487 and (D) cepharanthine. After a 48-h incubation period, the culture supernatants were collected and mixed with 22% (w/v) polyethylene glycol 6000 solution for 5 h. PERV particles were harvested by centrifugation of the mixture. The viral pellets were resuspended in lysis buffer and subjected to RT assay (lines). The viable cell number was determined by a tetrazolium dye cell proliferation assay (bars). Both the RT activity and cell proliferation assays were performed in duplicate. The data represent means plus ranges. Representative results for two independent experiments are shown.

bition of Tat functions. Furthermore, K-37 was reported to inhibit the gene expression of human T-lymphotropic virus type 1 (HTLV-1) in persistently infected cells (Wang et al., 2002a). Although the target molecule of K-37 still remains to be determined, the present observations for PERV suggest that K-37 may interact with a cellular factor or factors that play an important role in retroviral gene expression. It is assumed that K-37 inhibits an early stage of tran-

scriptional elongation of viral RNA (Okamoto et al., unpublished observations). EM2487 is a substance produced from a *Streptomyces* species and a potent and selective inhibitor of HIV-1 replication in acutely and chronically infected cells (Baba et al., 1999). Like K-37, EM2487 could inhibit HTLV-1 gene expression without affecting host cellular functions (Wang et al., 2002b). The chemical structures of K-37 and EM2487 are totally different from each other
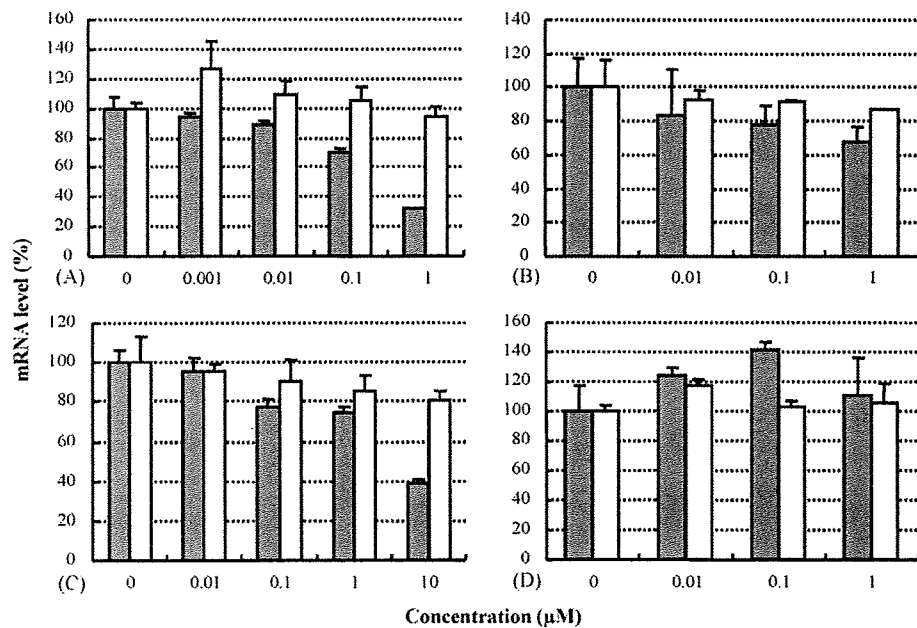
Fig. 3. Inhibitory effect of the test compounds on PERV mRNA synthesis in PK15 cells. PK15 cells were cultured in the presence of various concentrations of (A) K-37, (B) JTK-101, (C) EM2487 and (D) cepharanthine. After a 48-h incubation, the cells were collected, and total RNA was extracted. Quantitative real-time RT-PCR was performed to determine the amount of PERV mRNA in PK15 cells using a primer pair and probe specific to the PERV *pol* gene (gray columns). The inhibitory effect of the test compounds on host cellular mRNA synthesis was determined by quantitative RT-PCR for 18S mRNA (white columns). All experiments were performed in triplicate. The data represent means plus standard deviations. Representative results for two independent experiments are shown.

Table 1
Inhibitory effect of test compounds on PERV antigen production and mRNA synthesis in PK15 cells[a].

Compounds	PERV[b]			HIV-1[c]		HTLV-1[d]	
	EC_{50} (μM)	IC_{50} (μM)	CC_{50} (μM)	EC_{50} (μM)	CC_{50} (μM)	EC_{50} (μM)	CC_{50} (μM)
K-37	0.35 ± 0.04	0.34 ± 0.05	4.63 ± 1.62	0.033 ± 0.012	2.1 ± 0.3	0.44 ± 0.13	5.7 ± 1.0
EM2487	5.44 ± 1.40	4.36 ± 0.30	>10	0.075 ± 0.032	12.5 ± 4.1	3.6 ± 0.6	30.6 ± 3.5
JTK-101	>1	>1	2.18 ± 0.63	0.0014 ± 0.0005	3.8 ± 0.2	N.D.[e]	N.D.
Cepharanthine	>1	>1	4.39 ± 1.99	0.028 ± 0.016	1.3 ± 0.3	>3.0	3.0 ± 0.4

[a] Each experiment was carried out in duplicate or triplicate, and all data represent means ± ranges for two independent experiments.

[b] EC_{50}: 50% effective concentration based on the inhibition of PERV antigen production (RT) in culture supernatants of PK15 cells. IC_{50}: 50% inhibitory concentration based on the inhibition of PERV mRNA synthesis. CC_{50}: 50% cytotoxic concentration based on the inhibition of host cell proliferation.

[c] EC_{50}: 50% effective concentration based on the inhibition of HIV-1 antigen production (p24) in chronically infected cells. CC_{50}: 50% cytotoxic concentration based on the inhibition of host cell proliferation. Data are taken from the reports by Wang et al. (2007) for K-37 and JTK-101, Baba et al. (1999) for EM2487, and Baba et al. (2001) for cepharanthine.

[d] EC_{50}: 50% effective concentration based on the inhibition of HTLV-1 antigen production (p19) in infected cells. CC_{50}: 50% cytotoxic concentration based on the inhibition of host cell proliferation. Data are taken from the reports by Wang et al. (2002a) for K-37 and cepharanthine and Wang et al. (2002b) for EM2487.

[e] Not determined.

(Fig. 1), nevertheless they appear to share some common properties in antiretroviral activity and mechanism of action.

JTK-101 is a novel naphthalene derivative that inhibits HIV-1 replication in cell cultures (Wang et al., 2007). This compound was found to be highly active against HIV-1 in chronically infected cells but much less active in acutely infected cells. Studies of its mechanism of action suggested that JTK-101 exerted its anti-HIV-1 activity through the inhibition of CDK9/cyclin T1. Cepharantine is a plant alkaloid that has been shown to inhibit HIV-1 replication in a certain chronically infected cell line at low concentrations through the inhibition of NF-κB (Okamoto et al., 1998). Cepharanthine could also suppress stimulation-induced production of proinflammatory cytokines in human macrophages (Okamoto et al., 2001). This compound did not inhibit PERV replication in PK15 cells or even slightly enhanced it at the highest concentration tested (Fig. 2D).

The viral gene expression inhibitors K-37 and EM2487 may be able to keep PERV silent in porcine organs thereby reducing the risk of PERV transmission to recipients, which is never attainable with RT inhibitors. On the other hand, RT inhibitors are capable of inhibiting De Novo infection of recipients with PERV derived from porcine organs. Thus, an ideal strategy to prevent PERV transmission to organ recipients may be the combined treatment with an RT inhibitor for recipients and a gene expression inhibitor for donor organs. Unfortunately, the current gene expression inhibitors, such as K-37 or EM2487, may be toxic to human recipients at concentrations that completely suppress PERV production from donor cells or organs. Therefore, the optimization of their chemical structures would be required for the inhibition of PERV replication in vivo without generating serious side effects. Although the risk of PERV transmission upon xenotransplantation is supposed to be lower than initially thought, optimized retroviral gene expression inhibitors may be worth further pursuing for their potential efficacy in the clinical setting.

Acknowledgments

References

Allan, J.S., 2003. Understanding xenotransplantation risks from nonhuman primate retroviruses. Curr. Top. Microbiol. Immunol. 278, 101–123.

Baba, M., Okamoto, M., Kawamura, M., Makino, M., Higashida, T., Takashi, T., Kimura, Y., Ikeuchi, T., Tetsuka, T., Okamoto, T., 1998. Inhibition of human immunodeficiency virus type 1 replication and cytokine production by fluoroquinoline derivatives. Mol. Pharmacol. 53, 1097–1103.

Baba, M., Okamoto, M., Takeuchi, T., 1999. Inhibition of human immunodeficiency virus type 1 replication in acutely and chronically infected cells by EM2487,

a novel substance produced by a Streptomyces species. Antimicrob. Agents Chemother. 43, 2350–2355.

Baba, M., Okamoto, M., Kashiwaba, N., Ono, M., 2001. Anti-HIV-1 activity and structure–activity relationship of cepharanoline derivatives in chronically infected cells. Antiviral Chem. Chemother. 12, 307–312.

Cooper, D.K., Keogh, A.M., 2001. The potential role of xenotransplantation in treating endstage cardiac disease: a summary of the report of the Xenotransplantation Advisory Committee of the International Society for Heart and Lung Transplantation. Curr. Opin. Cardiol. 16, 105–109.

Heneine, W., Tibell, A., Switzer, W.M., Sandstrom, P., Rosales, G.V., Mathews, A., Korsgren, O., Chapman, L.E., Folks, T.M., Groth, C.G., 1998. No evidence of infection with porcine endogenous retrovirus in recipients of porcine islet-cell xenografts. Lancet 352, 695–699.

Louz, D., Bergmans, H.E., Loos, B.P., Hoeben, R.C., 2008. Reappraisal of biosafety risks posed by PERVs in xenotransplantation. Rev. Med. Virol. 18, 53–65.

Martin, U., Kiessig, V., Blusch, J.H., Haverich, A., von der Helm, K., Herden, T., Steinhoff, G., 1998. Expression of pig endogenous retrovirus by primary porcine endothelial cells and infection of human cells. Lancet 352, 692–694.

Okamoto, M., Ono, M., Baba, M., 1998. Potent inhibition of HIV type 1 replication by an anti-inflammatory alkaloid, cepharanthine, in chronically infected monocytic cells. AIDS Res. Hum. Retroviruses 14, 1239–1245.

Okamoto, M., Ono, M., Baba, M., 2001. Suppression of cytokine production and neural cell death by the anti-inflammatory alkaloid cepharanthine: a potential agent against HIV-1 encephalopathy. Biochem. Pharmacol. 62, 747–753.

Patience, C., Patton, G.S., Takeuchi, Y., Weiss, R.A., McClure, M.O., Rydberg, L., Breimer, M.E., 1998. No evidence of pig DNA or retroviral infection in patients with short-term extracorporeal connection to pig kidneys. Lancet 352, 699–701.

Patience, C., Takeuchi, Y., Weiss, R.A., 1997. Infection of human cells by an endogenous retrovirus of pigs. Nat. Med. 3, 282–286.

Paradis, K., Langford, G., Long, Z., Heneine, W., Sandstrom, P., Switzer, W.M., Chapman, L.E., Lockey, C., Onions, D., Otto, E., The XEN 111 Study Group, 1999. Search for cross-species transmission of porcine endogenous retrovirus in patients treated with living pig tissue. Science 285, 1236–1241.

Phan-Thanh, L., Kaeffer, B., Bottreau, E., 1992. Porcine retrovirus: optimal conditions for its biochemical detection. Arch. Virol. 123, 255–265.

Powell, S.K., Gates, M.E., Langford, G., Gu, M.-L., Lockey, C., Long, Z., Otto, E., 2000. Antiretroviral agents inhibit infection of human cells by porcine endogenous retroviruses. Antimicrob. Agents Chemother. 44, 3432–3433.

Qari, S.H., Magre, S., Garcia-Lerma, J.G., Hussain, A.I., Takeuchi, Y., Patience, C., Weiss, R.A., Heneine, W., 2001. Susceptibility of the porcine endogenous retrovirus to reverse transcriptase and protease inhibitors. J. Virol. 75, 1048–1053.

Shi, M., Wang, X., De Clercq, E., Takao, S., Baba, M., 2007. Selective inhibition of porcine endogenous retrovirus replication in human cells by acyclic nucleoside phosphonates. Antimicrob. Agents Chemother. 51, 2600–2604.

Wang, X., Miyake, H., Okamoto, M., Saito, M., Fujisawa, J., Tanaka, Y., Izumo, S., Baba, M., 2002a. Inhibition of the tax-dependent human T-lymphotropic virus type I replication in persistently infected cells by the fluoroquinolone derivative k-37. Mol. Pharmacol. 61, 1359–1365.

Wang, X., Okamoto, M., Kawamura, M., Izumo, S., Baba, M., 2002b. Inhibition of human T-lymphotropic virus type I gene expression by the Streptomyces-derived substance EM2487. Antiviral Chem. Chemother. 13, 177–183.

Wang, X., Yamataka, K., Okamoto, M., Ikeda, S., Baba, M., 2007. Potent and selective inhibition of Tat-dependent HIV-1 replication in chronically infected cells by a novel naphtalene derivative JTK-101. Antiviral Chem. Chemother. 18, 201–211.

Wilson, C.A., Wong, S., Muller, J., Davidson, C.E., Rose, T.M., Burd, P., 1998. Type C retrovirus released from porcine primary peripheral blood mononuclear cells infects human cells. J. Virol. 72, 3082–3087.

Yamamoto, O., Hamada, T., Tokui, N., Sasaguri, Y., 2001. Comparison of three in vitro assay systems used for assessing cytotoxic effect of heavy metals on cultured human keratinocytes. J. UOEH 23, 35–44.

Optical Response of Gold-Nanoparticle-Amplified Surface Plasmon Resonance Spectroscopy

Yuichi Uchiho,[†] Masayuki Shimojo,[‡,§] Kazuo Furuya,[§] and Kotaro Kajikawa[*,†]

Interdisciplinary Graduate School of Science and Engineering, Tokyo Institute of Technology, Nagatsuta, Midori-ku, Yokohama 226-8502, Japan, Advanced Science Research Laboratory, Saitama Institute of Technology, 1690 Fusaiji, Fukaya, 369-0293, Japan, and High Voltage Electron Microscopy Station, National Institute for Materials Science, 3-13 Sakura, Tsukuba, 305-0003, Japan

A simple formalism that predicts optical constants of a two-dimensionally distributed nanoparticle (NP) thin film is presented for analysis of the NP-amplified surface plasmon resonance. The dielectric constant of the NP thin film can be evaluated with simple expressions at low coverages (σ < 0.08), whereas the local fields induced by surrounding polarizations of NPs should be taken into account at coverages of σ > 0.08. Analytical and numerical calculations are carried out for evaluating the local fields at different conditions. The Clausius—Mossoti relation, which is usually used for evaluation of dielectric constants of a binary medium, does not hold in the NP thin films, because of the large interparticle distance and/or the retardation effect. We carried out SPR measurements for NP films with different NP coverages, and the results support the proposed analytical formalism. Finally we propose a procedure to evaluate the NP coverage from the NP-SPR profile experimentally obtained.

I. Introduction

Two-dimensionally distributed metallic nanoparticle (NP) films immobilized on a surface have been extensively studied as a promising material for localized surface plasmons (LSPs).[1-19] For instance, NP-amplified surface plasmon resonance (NP-SPR) delivers a great improvement on the protein detection limit of SPR biosensors using an attenuated total reflection(ATR) geometry.[20-29] In this technique, immobilization of NPs at proteins binding to ligand produces a great change in the resonance angle of incidence at the surface plasmon condition. We have also reported considerably enhanced second-harmonic generation (SHG) in two-dimensionally distributed gold NPs[7,8] and its application to biosensors.[9] The enhancement of SHG is due to the generation of intensified electric fields at the resonance condition of LSPs in metallic NPs.

Optical properties of the two-dimensionally distributed metallic nanoisland films formed on a substrate have been investigated since 1970s.[31-35] The nanoisland films were fabricated through thermal annealing of ultrathin metallic films vacuum-evaporated on a dielectric substrate. The nanoislands are approximated to be rotational ellipsoids, the optical properties of which were predicted taking into account the interaction from dipole array of surrounding nanoislands formed in the substrate, under the local field approximation (LFA). However their calculation is not straightforward for the analysis of practical applications such as the LSP biosensing. Well-defined chemically synthesized spherical NPs are recently commercially available for LSP, and they are easily immobilized on a substrate by surfactant or biological molecules. Thereby a simple formalism that predicts the optical properties of the NP films is necessary.

In this paper we present a theoretical expression for NP-SPR spectroscopy. We consider a film consisting of spherical NPs located above a metallic surface with a nanogap, as shown in Figure 1a. Although there are several approximation methods for evaluating a optical constant of a layer consisted of two different materials, such as the effective medium approximation, they cannot predict the NP-SPR profiles sufficiently (See Figure 1S in the Supporting Information). When the NPs are very close to a metallic surface, the electromagnetic interaction between the NP and the metallic surface is significant.[5-8,19,36-38] We calculated the NP-SPR profiles taking into account the interparticle interaction and the multipole interaction between the NP and the substrate. In order to verify the adequacy of our theoretical expressions, we performed experimental NP-SPR measurements to evaluate the optical parameters of the NP films. We obtained agreement between the experimental and the theoretical, and conclude that our theoretical expressions can be used to explain the optical response in the NP-SPR measurements.

II. Theory

A. Polarizability of NP. We consider a NP system consisting of an ambient medium (relative dielectric constant ε_1), a substrate (relative dielectric constant ε_2), and a spherical gold NP (radius R and relative dielectric constant ε_3), as illustrated in Figure 1a. The dielectric constants ε_2 and ε_3 are generally frequency dependent, whereas the dispersion of ε_1 is negligible. The gap is supported by a thin dielectric layer with a dielectric constant ε_4. While isolated spherical NPs are optically isotropic, they are usually uniaxial with the optic axis in the surface normal direction, z. The anisotropy originates from the electromagnetic interactions between the NP and the metallic substrate. Light is incident on the surface with the $x-z$ plane of incidence. Polarizability of a NP, α_q is generally described as

$$\alpha_q = 4\pi\varepsilon_1 R^3 A_q \qquad (q = // \text{ or } z) \qquad (1)$$

where $//$ denotes the in-plane components, namely x or y. There are a number of methods to evaluate the parameter A_q. They

---
* To whom correspondence should be addressed. E-mail: kajikawa@ep.titech.ac.jp.
  † Tokyo Institute of Technology.
  ‡ Saitama Institute of Technology.
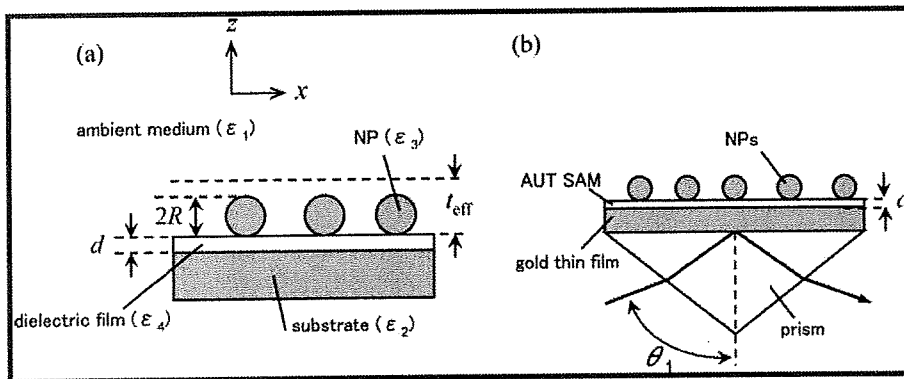 § National Institute for Materials Science.

Figure 1. (a) Schematic illustration of the NP thin film. (b) The optical geometry for SPR experiments.

differ in degree of approximation. When spherical NPs can be regarded as of isolation, the polarizability is isotropic and the subscript q is suppressed. The parameter A is described as

$$A = -\frac{\varepsilon_1 - \varepsilon_3}{2\varepsilon_1 + \varepsilon_3} \qquad (2)$$

In this expression, the contribution from the substrate and the supporting layer are ignored. Hence it is applied only to the limiting case that NPs are apart from the surface.

For calculating more accurate parameters of A, we need to consider the multipoles. This problem on the condition of $\varepsilon_4 = \varepsilon_1$ was solved by Wind et al.[38] We have slightly developed their formalism to take into account the contribution from the gap-supporting layer.[39] The jth order multipolar coefficients A_{qi} are calculated by the following equations:[2,38]

$$\sum_{j=1}^{\infty} \left\{ \delta_{kj} + \frac{k(\varepsilon_2 - \varepsilon_1)(\varepsilon_1 - \varepsilon_3)}{[k\varepsilon_3 + (k+1)\varepsilon_1](\varepsilon_1 + \varepsilon_2)} \frac{(k+j)!}{k!j!(2r_z)^{k+j+1}} \right\} A_{zj}$$

$$= \left(\frac{\varepsilon_1 - \varepsilon_3}{\varepsilon_1 + 2\varepsilon_3} \right) \delta_{k1} \qquad (k = 1, 2, 3, ...) \qquad (3)$$

$$\sum_{j=1}^{\infty} \left\{ \delta_{kj} + \frac{k(\varepsilon_2 - \varepsilon_1)(\varepsilon_1 - \varepsilon_3)}{[k\varepsilon_3 + (k+1)\varepsilon_1](\varepsilon_1 + \varepsilon_2)} \frac{(k+j)!}{(k+1)!(j-1)!(2r_{||})^{k+j+1}} \right\} A_{||j}$$

$$= \left(\frac{\varepsilon_1 - \varepsilon_3}{\varepsilon_1 + 2\varepsilon_3} \right) \delta_{k1} \qquad (k = 1, 2, 3, ...) \qquad (4)$$

where δ_{kj} is Kronecker's delta. Here, $r_z = 1 + (d\varepsilon_1)/(R\varepsilon_4)$ and $r_{||} = 1 + d/R$. The contribution of the gap layer is considered by using the thickness of the gap layer d divided by $\varepsilon_4/\varepsilon_1$ for the surface normal components of the electric fields. This is because the existence of the gap layer reduces the effective gap distance by a factor of $\varepsilon_4/\varepsilon_1$. The first order coefficient A_{q1} is responsible for the polarizability of NPs, i.e., $A_q = -A_{q1}$.

Figure 2 plots the real and imaginary parts of A_z and $A_{||}$ of the gold NPs on a gold surface in air, as a function of wavelength λ for different R/d values, using eqs 3 and 4. (See Figure 2S in Supporting Information for A_z and $A_{||}$ in water.) The multipoles until the 31st order were considered. The calculation was made with dielectric constants in literature.[40] The parameter A calculated by eq 2 corresponds to the profile at $R/d = 0$ because eq 2 is equivalent to the case of the infinity gap distance. At $R/d > 5$, another red-shifted band are observed as a sharp peak in the imaginary A_z profiles. The amount of redshift increases with R/d. Although the profiles in water are
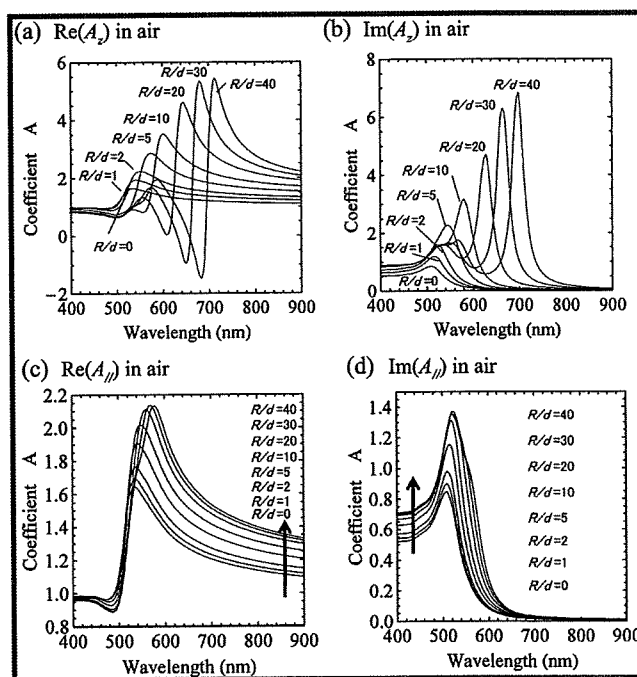

Figure 2. The parameter A_z and $A_{||}$ calculated using eqs 3 and 4 in air at different R/d ratios. (a) Real part of A_z. (b) Imaginary part of A_z. (c) Real part of $A_{||}$. (d) Imaginary part of $A_{||}$.
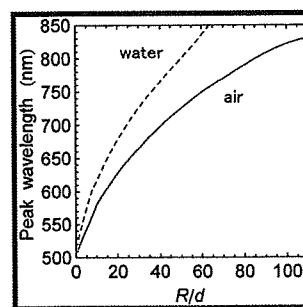

Figure 3. Peak wavelengths of the red-shifted band as a function of R/d for ambient of air and water.

similar to that in air, the amount of redshift in the imaginary A_z profiles in water is larger than that in air. Most $A_{||}$ spectra in air have a single peak at around 510 nm. In contrast to the A_z profiles, the red-shifted peak is observed only in the profiles at $R/d \geq 10$ in water and at $R/d = 40$ in air as a shoulder.

Figure 3 shows the peak wavelengths of the red-shifted band in the A_z curve, with respect to R/d in air or in water. The NPs supported by a dielectric thin film ($\varepsilon_4 = 2.25$) are considered. Similar relation was shown in previous papers, where the contribu-

4818 *J. Phys. Chem. C, Vol. 114, No. 11, 2010*

Uchiho et al.

tion of the gap layer was ignored[30] or was taken into account using the effective ambient dielectric constant of 2.0 instead of 1.0.[5,7,8] However, they can predict only resonance wavelengths with these parameters and cannot evaluate the polarizability.

B. Dielectric Constant of NP Film. Here we regard the metallic NPs dispersed on a substrate as a thin film having an effective thickness t_{eff}. The effective thickness t_{eff} is arbitrary within the range much less than the wavelength of light. We assume that the NPs are point dipoles in regard to the interparticle electromagnetic interaction and the interparticle multipolar interaction is ignored. This is because the interparticle distance is usually large enough and the coverages of NPs in our experiments are low enough to satisfy this approximation. A detailed discussion of the interparticle interaction can be found in section II.C. The contribution of the mirror images formed in the substrate is taken in the parameter A. As a result, we can simply describe the optical properties of the spherical NP films as described below.

The polarization of a NP, **p**, induced by a local electric field, $\mathbf{E}_{\text{loc}}$, is written as

$$\mathbf{p} = \varepsilon_0 \overset{\leftrightarrow}{\alpha} \mathbf{E}_{\text{loc}} \tag{5}$$

where $\overset{\leftrightarrow}{\alpha}$ is a polarizability tensor of the NP and ε_0 is the vacuum permittivity. The tensor $\overset{\leftrightarrow}{\alpha}$ is diagonal and has two independent components $\alpha_{//} = \alpha_{xx} = \alpha_{yy}$ and $\alpha_z = \alpha_{zz}$, since NPs are generally uniaxial with the optic axis in the surface normal direction. The local field $\mathbf{E}_{\text{loc}}$ at the original point generally differs from the external electric field $\mathbf{E}_{\text{ext}}$ of the incident light and is described as[41-43]

$$\mathbf{E}_{\text{loc}} = \mathbf{E}_{\text{ext}} + \frac{1}{4\pi\varepsilon_0\varepsilon_1}\sum_i \left(\frac{3\mathbf{n}_i\mathbf{n}_i - 1}{r_i^3}\right)\mathbf{p}_i \tag{6}$$

Here $\mathbf{n}_i$ is the unit vector pointing from a surrounding dipole i (dipole moment $\mathbf{p}_i$) to the original point and r_i is the distance between the dipole and the original point. Since each dipole is considered to be equivalent, we can use the LFA. Then the local field $\mathbf{E}_{\text{loc}}$ can be written as

$$\mathbf{E}_{\text{loc}} = \mathbf{E}_{\text{ext}} + \frac{1}{4\pi\varepsilon_0\varepsilon_1}\overset{\leftrightarrow}{\Xi}\mathbf{p} \tag{7}$$

The tensor $\overset{\leftrightarrow}{\Xi}$ is an operator to sum up the electric fields induced by the surrounding dipoles. A local field factor tensor $\overset{\leftrightarrow}{L}$ is introduced to connect them as $\mathbf{E}_{\text{loc}} = \overset{\leftrightarrow}{L}\mathbf{E}_{\text{ext}}$. The $\overset{\leftrightarrow}{L}$ tensor is diagonal and generally has three independent components L_{xx}, L_{yy}, and L_{zz}, and using eqs 5 and 7, $\overset{\leftrightarrow}{L}$ is written as

$$\overset{\leftrightarrow}{L} = \left(\overset{\leftrightarrow}{I} - \frac{1}{4\pi\varepsilon_1}\overset{\leftrightarrow}{\Xi}\overset{\leftrightarrow}{\alpha}\right)^{-1} \tag{8}$$

where $\overset{\leftrightarrow}{I}$ is the unit tensor. The tensor $\overset{\leftrightarrow}{\Xi}$ is diagonal and generally has three independent components Ξ_{xx}, Ξ_{yy} and Ξ_{zz}. Details of the tensor $\overset{\leftrightarrow}{\Xi}$ is discussed in the next section.

The macroscopic polarization **P** can be expressed as

$$\mathbf{P} = N\mathbf{p} \tag{9}$$

where N is a volume number density of polarization. The surface number density, N_s, is more essential than N for two-dimensional systems. Hence we will use N_s instead of N, using the relation $N_s = t_{\text{eff}}N$.

The flux density of NPs layer, **D**, can be expressed as

$$\mathbf{D} = \varepsilon_0\varepsilon\mathbf{E} = \varepsilon_0\varepsilon_1\mathbf{E} + \mathbf{P} \tag{10}$$

where **E** represents the electric field of the NP layer and ε represents the dielectric tensor of the NP layer. We added ε_1 in eq 10 because without any NPs ($\mathbf{P} = 0$), the dielectric constant, ε, should be same as that of an ambient medium, ε_1. Then eq 10 can be transformed as following expression using eqs 5, 7, and 9.

$$\begin{aligned}\varepsilon_0\varepsilon\mathbf{E} &= \varepsilon_0\varepsilon_1\mathbf{E} + N\varepsilon_0\overset{\leftrightarrow}{\alpha}\mathbf{E}_{\text{loc}} \\ &= \varepsilon_0\varepsilon_1\mathbf{E} + N\varepsilon_0\overset{\leftrightarrow}{\alpha}\overset{\leftrightarrow}{L}\mathbf{E}_{\text{ext}}\end{aligned} \tag{11}$$

Since the surface normal component of electric flux density is continuous at the boundary ($\varepsilon_z E_z = \varepsilon_1 E_{\text{ext},z}$), we have the surface normal component of the relative dielectric constant of the NP film, ε_z, as

$$\varepsilon_z = \varepsilon_1\left(1 - \frac{1}{\varepsilon_1}N\alpha_z L_{zz}\right)^{-1} = \varepsilon_1\left(1 - \frac{1}{\varepsilon_1}\left(\frac{N_s}{t_{\text{eff}}}\right)\alpha_z L_{zz}\right)^{-1} \tag{12}$$

The continuity of the in-plain electric field ($E_{//} = E_{\text{ext},//}$) yields the in-plain component, $\varepsilon_{//}$,

$$\varepsilon_{//} = \varepsilon_1 + N\alpha_{//}L_{//} = \varepsilon_1 + \left(\frac{N_s}{t_{\text{eff}}}\right)\alpha_{//}L_{//} \tag{13}$$

Although t_{eff} is arbitrary, one of the most reasonable and convenient choice is $t_{\text{eff}} = 2R$. Then we can directly relate the dielectric constant of the thin film to the coverage of the NPs, σ, using the relation $\sigma = N_s\pi R^2$ and eq 1. Then, eq 12 is rewritten as

$$\varepsilon_z = \varepsilon_1\left(1 + \frac{2\sigma A_z L_{zz}}{1 - 2\sigma A_z L_{zz}}\right) \tag{14}$$

and similarly eq 13 is

$$\varepsilon_{//} = \varepsilon_1(1 + 2\sigma A_{//}L_{//}) \tag{15}$$

C. Ξ Components. First we consider the tensor $\overset{\leftrightarrow}{\Xi}$ in the absence of retardation. When NPs are too close (the gap between the NPs is less than the diameter of the particles: $a < 4R$ in square lattice), the interparticle multipolar interaction cannot be neglected and the local field cannot be written by the simple dipolar form written by eq 6. This is the case that $\sigma > \pi R^2/(4R)^2 \sim 0.2$. Thus we will treat the case that the interparticle multipolar interaction can be neglected ($\sigma < 0.2$), hereafter.

For a two-dimensional square lattice with a lattice constant a ($a > 4R$), the tensor $\overset{\leftrightarrow}{\Xi}^{\text{sq}}$ is composed of two independent diagonal components[41-43]

$$\Xi_x^{\text{sq}} = \Xi_{zz}^{\text{sq}} = \frac{\xi_z^{\text{sq}}}{a^3} = (N_s^{\text{sq}})^{3/2}\xi_z^{\text{sq}} \tag{16}$$

Optical Response of NP-SPR

J. Phys. Chem. C, Vol. 114, No. 11, 2010 **4819**

and

$$\Xi_{//}^{sq} = \Xi_{xx}^{sq} = \Xi_{yy}^{sq} = \frac{\xi_{//}^{sq}}{a^3} = (N_s^{sq})^{3/2}\xi_{//}^{sq} \qquad (17)$$

where the relation $N_s^{sq} = a^{-2}$ was used. The ξ values for a square lattice are given in literature:[44] $\xi^{sq} = -9.034$ and $\xi_{//}^{sq} = -\xi_z^{sq}/2$. The parameters for a hexagonal lattice with a lattice constant a are also given: $\xi_z^{hex} = -11.034$ and $\xi_{//}^{hex} = -\xi_z^{hex}/2$. The relation $N_s^{hex} = (2/\sqrt{3})(1/a^2)$ allows us to give the component Ξ_q^{hex}

$$\Xi_q^{hex} = \frac{\xi_q^{hex}}{a^3} = \left(\frac{\sqrt{3}}{2}N_s^{hex}\right)^{3/2}\xi_q^{hex} \cong (N_s^{hex})^{3/2}\xi_q^{sq}$$

$$(q = // \text{ or } z) \qquad (18)$$

Equation 18 implies that the Ξ components solely depend on N_s and ξ_q^{sq}. To verify this, we evaluated Ξ components in a two-dimensional system consisting of randomly distributed NPs. The procedure of the calculation is as follows: (1) A square with a dimension of 202×202 is considered. A NP of unity diameter is put at the center of the square, which is defined as the original point. (2) NPs of unity diameter are randomly placed on the square to make the interparticle distances be more than twice the diameter of the NP, in order to neglect the interparticle multipolar interaction. (3) The NP at the original point is removed, and the electric fields at the original point induced by the surrounding dipoles are summed up to have the tensor Ξ. In this calculation, 2×10^5 positions are randomly generated, and 6278 ± 14.8 NPs are placed without overlapping. This corresponds to $N_s^{ran} = 0.1539 \pm 0.000363$ and the corresponding coverage $\sigma = 0.1233 \pm 0.00029$. Iteration of 10 times yields the mean values of Ξ: $\Xi_{//}^{ran} = 0.268 \pm 0.138$ and $\Xi_z^{ran} = -0.5634 \pm 0.0739$. The distribution of the in-plane component $\Xi_{//}^{ran}$ is almost twice as large as that of the normal component Ξ_z^{ran}. This is because the in-plane component is strongly affected by the position of adjacent surrounding dipoles. With these results, we have the relations

$$\Xi_z^{ran} = -0.5634 \cong (N_s^{ran})^{3/2}\xi_z^{sq} \qquad (19)$$

and

$$\Xi_{//}^{ran} = 0.268 \cong (N_s^{ran})^{3/2}\xi_{//}^{sq} \qquad (20)$$

These results allow us to conclude that Ξ solely depends on N_s, and that one may use a two-dimensional square lattice without losing generality for evaluation of the Ξ tensor components.

Next, we consider the retardation effect. We only consider the square lattice below since it can be used as a general case. We performed numerical calculations for square lattice having 4×10^5 (201×201) dipoles to evaluate ξ components. The incident light at wavelength λ is directed onto the surface, where the plane of incidence is $x-z$ plane. The electric fields at the original point induced by the surrounding dipoles are added and complex ξ values are calculated. Because of the retardation effect, the in-plane components ξ_x and ξ_y are different; there are generally three independent ξ components. The ξ values are plotted as a function of λ/a at $0°$ and $45°$ angles of incidence in Figure 4. At normal incidence ξ_x and ξ_y are degenerated. In
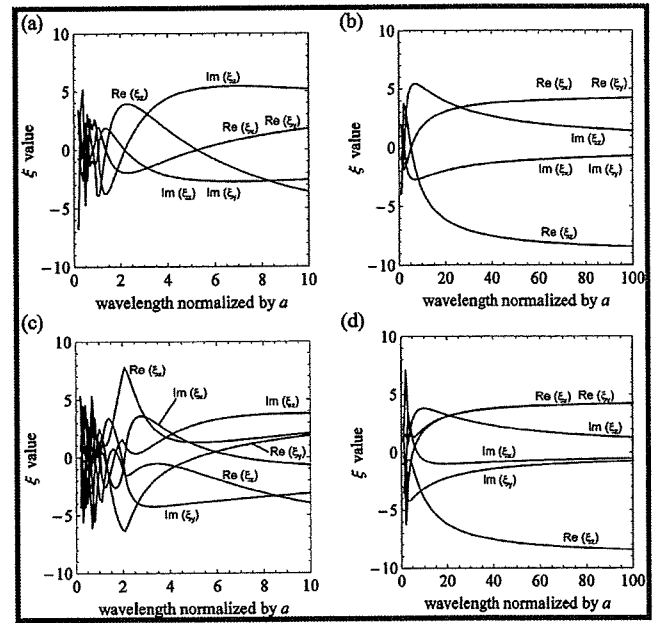
Figure 4. The parameter ξ including the retardation effect, as a function of normalized wavelength λ/a. (a) The ξ parameter at wavelengths $0 < \lambda/a < 10$ at normal incidence. (b) The ξ parameter at wavelengths $0 < \lambda/a < 100$ at normal incidence. (c) The ξ parameter at wavelengths $0 < \lambda/a < 10$ at $45°$ angle of incidence. (d) The ξ parameter at wavelengths $0 < \lambda/a < 100$ at $45°$ angle of incidence.
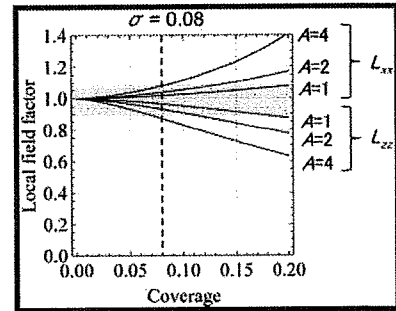
Figure 5. Local field factor as a function of coverage at different A values.

the region $(\lambda/a) \geq 50$, the retardation effect is so small that we can use the static ξ values, $\xi_z^{sq} = -2\xi_{//}^{sq} = -9.034$. However this is only limited cases that small NPs ($R \lesssim 3$ nm) are distributed with coverages $\sigma \leq 0.2$. In region $(\lambda/a) \leq 50$, the ξ values are complex and considerably depend on the value (λ/a). Therefore the ξ values should be calculated in general. However as described in the next section, we can regard the local field factor to be unity at coverages $\sigma \leq 0.08$. Therefore the ξ values including the retardation effect is needed in the cases that $0.08 \leq \sigma \leq 0.2$.

D. NP Film at Low Coverage. Using the relation, $\sigma = N_s\pi R^2$, and eq 8, L_{ii} is written as

$$L_{ii} = \left(1 - \left(\frac{\sigma}{\pi}\right)^{3/2}\xi_i^{sq}A_i\right)^{-1} \qquad (i = x, y \text{ or } z) \qquad (21)$$

Figure 5 shows the local field factors calculated as a function of σ at various A values, using eq 21. Since the parameter A is usually less than 2 under off-resonance conditions and the static ξ^{sq} values are the maximum, one may use the local field factor $L_q \sim 1$ for $\sigma < 0.08$ within deviation of 10%. At this low

4820 *J. Phys. Chem. C, Vol. 114, No. 11, 2010*

Uchiho et al.

coverage, eqs 14 and 15 can be written in the following simple forms

$$\varepsilon_z = \varepsilon_1\left(1 + \frac{2\sigma A_z}{1 - 2\sigma A_z}\right) \tag{22}$$

and

$$\varepsilon_{//} = \varepsilon_1(1 + 2\sigma A_{//}) \tag{23}$$

The dielectric constants of a NP film are described as a function of the parameters A and σ.

E. Comparison with the Clausius—Mossoti Relation.

Substituting eq 21 into eq 12, the dielectric constant ε_z is written

$$\varepsilon_z \doteq \frac{\varepsilon_1\left(1 - \frac{N_s^{3/2}\xi_z\alpha_z}{4\pi\varepsilon_1}\right)}{1 - \frac{N_s^{3/2}\xi_z\alpha_z}{4\pi\varepsilon_1} - \frac{N_s\alpha_z}{t_{eff}\varepsilon_1}} = \frac{\varepsilon_1\left(1 - \left(\frac{\sigma}{\pi}\right)^{3/2}\xi_z A_z\right)}{1 - \left(\frac{\sigma}{\pi}\right)^{3/2}\xi_z A_z - 2\sigma A_z} \tag{24}$$

Similary, substituting eq 21 into eq 13, the dielectric constant $\varepsilon_{//}$ is written

$$\varepsilon_{//} = \frac{\varepsilon_1 - \frac{N_s^{3/2}\xi_{//}\alpha_{//}}{4\pi} + \frac{N_s}{t_{eff}}\alpha_{//}}{1 - \frac{N_s^{3/2}\xi_{//}\alpha_{//}}{4\pi\varepsilon_1}}$$

$$= \frac{\varepsilon_1\left(1 - \left(\frac{\sigma}{\pi}\right)^{3/2}\xi_{//}A_{//} + 2\sigma A_{//}\right)}{1 - \left(\frac{\sigma}{\pi}\right)^{3/2}\xi_{//}A_{//} - 2\sigma A_{//}} \tag{25}$$

Ui et al. reported that the relations are approximated to the Clausius—Mossoti relation if one sets $t_{eff} = a$ in the absence of the retardation effect.[43] With $t_{eff} = a$, eqs 24 and 25 are reduced to

$$\varepsilon_z = \varepsilon_1\frac{1 - \left(\frac{\xi_z}{4\pi}\right)\frac{N\alpha_z}{\varepsilon_1}}{1 - \left(\frac{\xi_z}{4\pi} + 1\right)\frac{N\alpha_z}{\varepsilon_1}} \sim \varepsilon_1\frac{1 + \frac{2}{3}\frac{N\alpha_z}{\varepsilon_1}}{1 - \frac{1}{3}\frac{N\alpha_z}{\varepsilon_1}} \tag{26}$$

and

$$\varepsilon_{//} = \varepsilon_1\frac{1 + \left(1 - \frac{\xi_{//}}{4\pi}\right)\frac{N\alpha_{//}}{\varepsilon_1}}{1 - \left(\frac{\xi_{//}}{4\pi}\right)\frac{N\alpha_{//}}{\varepsilon_1}} \sim \varepsilon_1\frac{1 + \frac{2}{3}\frac{N\alpha_{//}}{\varepsilon_1}}{1 - \frac{1}{3}\frac{N\alpha_{//}}{\varepsilon_1}} \tag{27}$$

Then the two-dimensional polarization sheet can be regarded as a slice of bulk with a thickness of a, having the same dielectric constant as that of bulk. This argument is useful for

monomolecular layers, but is not applicable to NP films, because of the large interparticle distance (<100 nm) and the retardation effect. Accordingly, application of the Clausius-Mossoti relation to NP systems is usually irrelevant.

F. Effective Dielectric Constant of NP Film with Anisotropy.

Since the procedure described above predicts the dielectric constant of the NP film, we can calculate the optical response using the transfer matrix method which is usually used for multilayer systems. The NP film is generally uniaxial with the optic axis in the surface normal direction. Hence we can use the transfer matrix method for isotropic medium by using the effective dielectric constant of the uniaxial NP layer ε_{NP}

$$\varepsilon_{NP} = \frac{\varepsilon_z\varepsilon_{//} + \varepsilon_1\sin^2\theta_1(\varepsilon_z - \varepsilon_{//})}{\varepsilon_z} \tag{28}$$

where ε_{NP} varies with the angle of incidence, θ_1. For fitting of the experimental SPR curve to the theoretical one, ε_{NP} can be written by the parameters A and σ.

$$\varepsilon_{NP} = \varepsilon_1(1 + 2\sigma A_{//} + \sin^2\theta_1(2\sigma(A_z - A_{//}) + 4\sigma^2 A_z A_{//}))$$
$$\cong \varepsilon_1(1 + 2\sigma(A_{//}\cos^2\theta_1 + A_z\sin^2\theta_1)) \tag{29}$$

The approximation $4\sigma^2 A_z A_{//} = 0$ is valid for small σ. Then the SPR curve can be fitted with the single parameter of σ, since A_z, $A_{//}$ and $t_{eff} = 2R$ are known.

III. Calculation

On the basis of the analytical expressions described above, we computed the SPR profiles using the transfer matrix method.[45] First we calculated reflectivity of NP (5 nm in diameter) films supported by a gap-supporting layer 5 nm thick ($\varepsilon_4 = 2.25$), which is the typical dimension of proteins. The gap-supporting layer is placed on a 50 nm-thick gold film deposited at the bottom of a rectangular glass prism (refractive index 1.5). For evaluation of the dielectric constant of the NP film, the parameters of A were calculated using eq 2, which are plotted in Figure 2. This is good approximation to the case that the NP diameter is less than 10 nm, since the A profiles of eq 2 are similar to those of eq 3 and eq 4 at $R/d \le 1.0$, within an error of less than 5%. We consider an incomplete gap-supporting layer (submonolayer) with the effective dielectric constant, $\varepsilon_{4,eff}$, at coverage σ, which is estimated by the following expression:

$$\varepsilon_{4,eff} = \sigma\varepsilon_4 + (1 - \sigma)\varepsilon_1 \tag{30}$$

where ε_4 (= 2.25) is the relative dielectric constant of the complete gap-supporting layer (see Figure 3S in the Supporting Information about comparison between eq 30 and effective medium approximation, and little difference exists between the dielectric constants by the two methods). For simplicity, the coverage of the gap-supporting material and the NPs was assumed to be identical. Figure 6 plots the SPR profiles at different NP coverages and at wavelength 635 nm in air (See Figure 4S in the Supporting Information for different wavelength 835 nm and water). The resonance angle increases with σ, and the minimum reflectivity almost stays zero at any σ values. This SPR shift is due to the increase in the real part of ε_{NP}. The amount of the SPR shift in water is slightly larger than those in air. In the profiles of 835 nm, the amount of the SPR shifts is
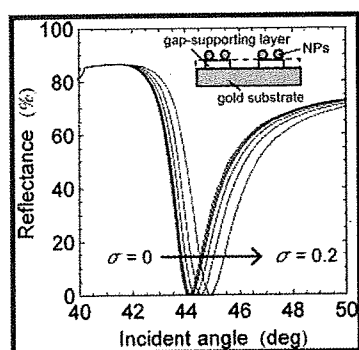
Optical Response of NP-SPR

J. Phys. Chem. C, Vol. 114, No. 11, 2010 **4821**

Figure 6. Calculated SPR profiles at different coverages $\sigma = 0, 0.01, 0.02, 0.05, 0.1$, and 0.2 at $\lambda = 635$ nm in air.
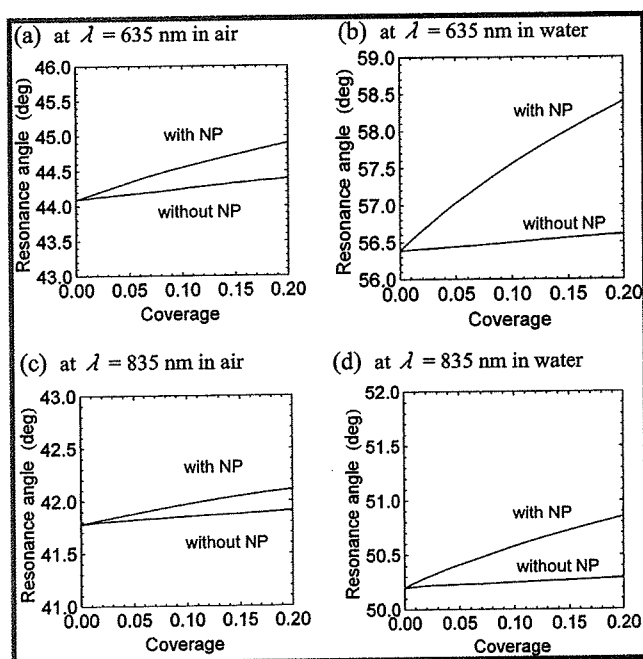

Figure 7. Resonance angles as a function of coverage, at $\lambda = 635$ nm in air (a), $\lambda = 635$ nm in water (b). $\lambda = 835$ nm in air (c), and $\lambda = 835$ nm in water (d).

Figure 8. Calculated SPR profiles at different coverages $= 0, 0.01, 0.03, 0.05, 0.1$, and 0.2 at $= 635$ nm in air. The thickness of the gap-supporting layer $d = 5$ nm and $R = 25$ nm.

TABLE 1: Mean Change in the Resonance Angle of the Films with or without NPs[a]

wavelength (nm)	ambient	NPs	$\Delta\theta_r/\Delta\sigma$ deg
635	air	w/o	1.5
635	air	w	4.05
635	water	w/o	1.1
635	water	w	10.05
835	air	w/o	0.65
835	air	w	1.65
835	water	w/o	0.45
835	water	w	3.25

[a] The NPs are assumed to be isolated and eq 2 was used for calculation of A. "w" and "w/o" in the NPs column mean "with NPs" and "without NPs", respectively.

smaller than that of the corresponding shifts at 635 nm. In either case, the obvious broadening in the SPR dip is not observed which has been often reported. This is because the electromagnetic interaction between the NP and the substrate, which is the origin of the broadening, is not taking into account in this calculation.

The resonance angles, θ_r, are plotted as a function of the NP coverage in Figure 7. The resonance angles in the absence of NPs are also plotted, in which the effective dielectric constant of the gap-supporting layer is calculated using eq 30. The NP-SPR at 635 nm in air shows a shift of 0.81 degree at $\sigma = 0.2$, whereas the shift due to presence of 5 nm dielectric film at the same coverage is only 0.30 degrees in the absence of NPs. This means that the sensitivity is enhanced by a factor of 2.7 on adsorption of NPs. The mean change rates of the resonance angle with respect to the coverage, $\Delta\theta_r/\Delta\sigma$, are listed in Table 1 at various conditions. The rate is defined as

$$\frac{\Delta\theta_r}{\Delta\sigma} = \frac{\theta_r(\sigma_1) - \theta_r(0)}{\sigma_1} \quad (31)$$

We calculated with $\sigma_1 = 0.2$; unless the SPR dip disappears at high coverage for heavy broadening, where the highest σ_1
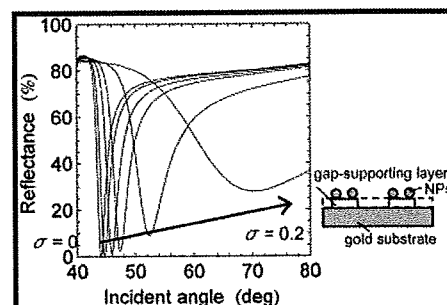
that gives a SPR dip was used. The enhancement factors are about 2—3 in air and 7—10 in water. This is in agreement with the results in the previous study, in which NPs ($R = 5$ nm) were used to intensify the signal from IgG.[21]

Next we computed the SPR profiles, taking into account the contribution of the substrate. Figure 8 shows the SPR profiles of the NP films at $R = 25$ nm, and $\lambda = 635$ nm (see Figure 5S for different sizes of NPs). The gap-supporting layer 5 nm thick is considered. The local field factor L_q is unity in the case of $\sigma \leq 0.08$, as described in Section II D. In the case of $0.08 \leq \sigma \leq 0.2$, we calculated the ξ components for the incident angles with taking into account the retardation effect as described in section II.C. Both broadening and an increase in the minimum reflectivity are observed in the profiles at $R = 25, 40$, and 75 nm at high coverages. This is due to a large imaginary part of the dielectric constant of the NP film. The calculated resonance angle, θ_r, is plotted as a function of the coverage at $R = 5, 15, 25, 40$, and 75 nm in Figure 9. It should be noted that, although long-wavelength approximation (retardation effect) is not held for $R = 75$ nm, we show the results of $R = 75$ nm since they are qualitatively adequate. The θ_r profiles at 635 nm in air and in water are shown in Figure 9, panels a and b, respectively, and the profiles at 835 nm in air and in water are shown in Figure 9, panels c and d. At a given coverage, large NPs give a great change in θ_r. This is due to the large effective thickness, $2R$ and the large real part of A. However, the broader SPR dip with negative shift in water at $R = 75$ nm and $\lambda = 635$ nm are observed, as increasing the coverage (Figure 10a). This strange behavior is caused by the small negative real part of A_z at $\lambda = 635$ nm and $R/d = 15$ as shown in the spectrum of parameter A_z (Figure 10b). The mean rates of $\Delta\theta_r/\Delta\sigma$ are listed in Table 2 at different R values. Mostly the rate increases with NP size. The largest rate 433 is given at $R = 75$ nm and $\lambda = 635$ nm. The electromagnetic interaction between the NPs and the substrate produces the great enhancement in NP-SPR.
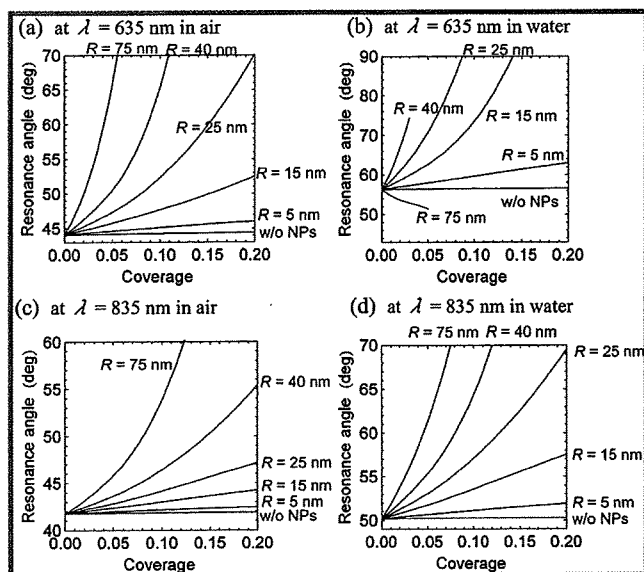
Figure 9. Resonance angle as a function of coverage for different R. (a) $\lambda = 635$ nm in air, (b) $\lambda = 635$ nm in water, (c) $\lambda = 835$ nm in air, and (d) $\lambda = 835$ nm in water.
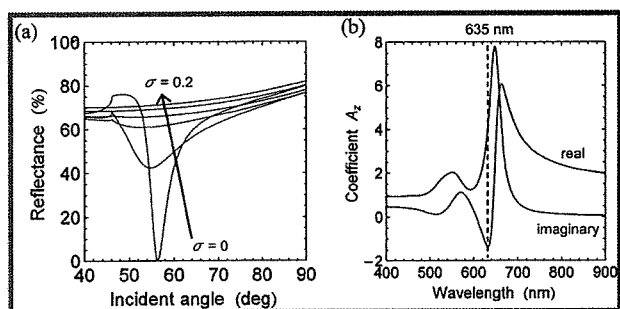

Figure 10. (a) Calculated SPR profiles ($R = 75$ nm) at different coverages $\sigma = 0, 0.01, 0.03, 0.05, 0.1$, and 0.2 at $\lambda = 635$ nm in water. The thickness of the gap-supporting layer $d = 5$ nm. (b) The parameter A_z calculated at $R/d = 15$.

According to the calculated results, we found the conditions that give a large enhancement of the NP-SPR. Larger NP sizes give greater enhancement of the SPR signal unless the LSP is on resonance at the illumination light wavelength. If the LSP is on resonance, the peak shift upon adsorption or binding to the analyte is not great because of the small real part of the polarizability. To avoid this, we had better use an illumination wavelength in near-infrared region, for instance, using a semiconductor laser line at 835 nm.

IV. Experimental Section

The sample used in this study is illustrated in Figure 1b. Thin gold films were prepared on a silica slide used as a substrate by vacuum evaporation at a pressure of 10^4 Pa. A 1 nm-thick chromium thin film was deposited between the gold film and the silica slide to promote adhesion of the gold film to the substrate. The 11-amino-1-undecanethiol (AUT) self-assembled monolayer (SAM) purchased from Dojindo Laboratory, Japan was dissolved in ethanol at a concentration of 0.1 mM. Successively AUT SAMs were prepared by immersion of the gold substrate in the solution for 1 h, followed by rinsing with ethanol. The AUT-covered gold substrate was immersed in an aqueous solution of gold NPs 50 nm in diameter (Tanaka Kikinzoku K.K., Japan). The samples were prepared with immersion time of 30, 300, and 3000 s. The substrate was then

TABLE 2: Mean Change in the Resonance Angle of the NP Films[a]

wavelength (nm)	ambient	R (nm)	$\Delta\theta_r/\Delta\sigma$ deg
635	air	w/o	1.5
635	air	5	9.55
635	air	15	42.2
635	air	25	131.1
635	air	40	213.2
635	air	75	433
635	water	w/o	1.1
635	water	5	32.85
635	water	15	168.9
635	water	25	287.8
635	water	40	598
635	water	75	−98.8
835	air	w/o	0.65
835	air	5	3.5
835	air	15	12.45
835	air	25	27.05
835	air	40	68.35
835	air	75	120.3
835	water	w/o	0.45
835	water	5	8.6
835	water	15	36.75
835	water	25	96.65
835	water	40	141.2
835	water	75	221.6

[a] The NPs (radius R) are assumed to be located above a gold surface with a gap distance of 5 nm. Equations 3 and 4 were used for calculation of A. "w/o" in the R column means "in the absence of NPs".

rinsed with pure water. A field emission scanning electron microscope (FE-SEM) was used to evaluate the surface number density of the gold nanoparticles.

The SPR spectroscopy was carried out in the attenuated total reflection (ATR) geometry. A rectangular BK7 prism was used for the coupling of surface plasmons. Two kinds of semiconductor lasers (635 and 835 nm) were used. A couple of polarizers were used to choose the illumination polarization and to control the illumination intensity. The reflected light was detected with a silicon photodiode, and the signal was recorded with a 12-bit A/D converter board installed in a computer that controlled the sample stages.

V. Results and Discussion

In order to test the theory described above, we performed SPR measurements for the samples having different NP coverages. Figure 11 shows the SEM images of the samples prepared for different immersion times 30 s, 300 and 3000 s. They are respectively denoted as sample I, II and III. The coverages of NPs were evaluated from the SEM images and are summarized in Table 3. The images show that the interparticle distances are enough to neglect the interparticle interactions, which is not significant when $\sigma < 0.2$. Hence the small coverage in each sample allows us to use the simple formalism given in eq 22 and eq 23.

The NP-SPR curves were captured at 635 nm for samples I–III. Figure 12a shows the SPR curve for an AUT-covered thin gold film in the absence of NPs, for reference. The experimental curves for samples I–III are shown with solid lines in Figure 12b–d (see also Figure 1S in the Supporting Information for the calculation results by effective medium approximation). To calculate the parameter A_q for samples I–III, the gap distance d was estimated with the p-polarized transmission absorption spectra at 60° incidence. From the absorption
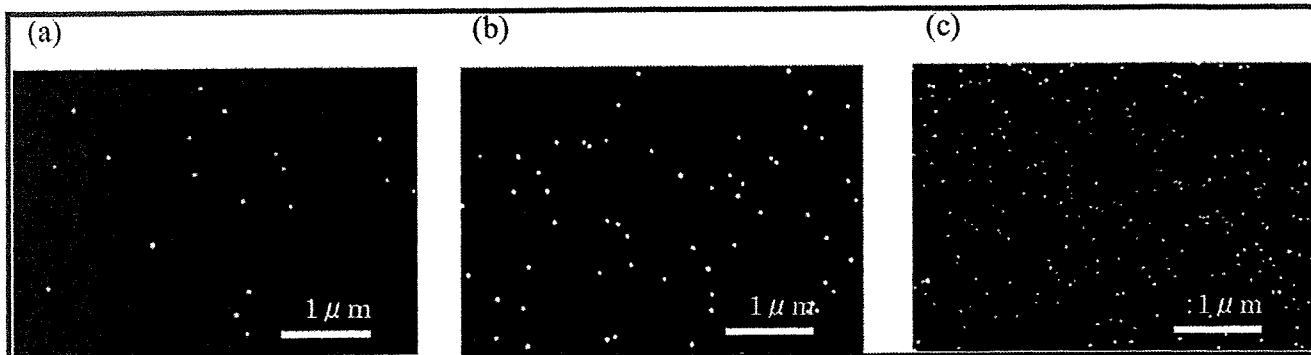
Optical Response of NP-SPR

J. Phys. Chem. C, Vol. 114, No. 11, 2010 **4823**

Figure 11. SEM images for immersion time (a) 30, (b) 300, and (c) 3000 s.

TABLE 3: Coverages Evaluated by SEM Microscopy and Dielectric Constants of the NP Films for Each Sample

sample	coverage σ	ε_z	$\varepsilon_{//}$
I	0.0023	$1.00143 + 0.00367i$	$1.00401 + 0.00022i$
II	0.0075	$1.00451 + 0.00120i$	$1.01290 + 0.00071i$
III	0.032	$1.01650 + 0.05390i$	$1.05460 + 0.00293i$

spectrum, the evaluated gap distance of the AUT SAM to be 0.75 nm and its standard deviation of 0.21 nm was used. The details to determine these parameters are described in a previous paper.[39] Then assuming the normal distribution of the gap distance, the SPR curves were calculated by the transfer matrix method, as shown with broken lines in Figure 12b–d. One may see the agreement on the resonance angles between the experiments and the calculations. This indicates that this theory is applicable to evaluate the dielectric constant of NP film. The resonance angle scarcely changes in spite of the increase in σ. This is because the real part of A_z is small at $R/d = 33$ and the real part of ε_z is almost unchanged with σ, as shown in the calculated A_z spectrum (Figure 13a). On the other hand, the imaginary part of ε_z increases with σ, resulting in the broadening of the SPR dip.

Figure 13. The parameter A calculated at $R/d = 33$. (a) In-plain component $A_{//}$ and (b) normal component A_z.
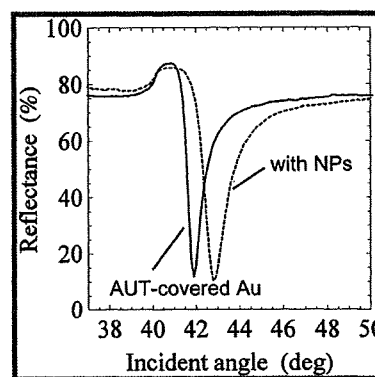
Figure 14. SPR profile measured for sample IV. (a) without any NP film (b) with the NP film.

In order to support the results shown above, we prepared another sample prepared in the same manner as we did for sample III (denoted as sample IV). Figure 14 shows the SPR profiles at 835 nm for sample IV and the gold thin film in the absence of NPs. On the contrary to the SPR profiles at 635 nm, the SPR dip is shifted to larger incident angle without broadening. This is due to the small imaginary part of the parameter A at 835 nm, as shown in Figure 13. Since the parameter A_q is obtained, we can obtain σ from the SPR curve. The coverage was evaluated to be 0.036 and this was almost same as that of sample III. The SPR profile at 835 nm shows a obvious shift of the resonance angle compared to that of 635 nm since the wavelength of 835 nm is on off-resonance (Figure 13b).

VI. Conclusion

A simple formalism that predicts optical constants of a two-dimensionally distributed NP thin film is presented. The dielectric constant can be evaluated with the simple expressions given in eqs 22 and 23, at low coverages ($\sigma < 0.08$). Otherwise,
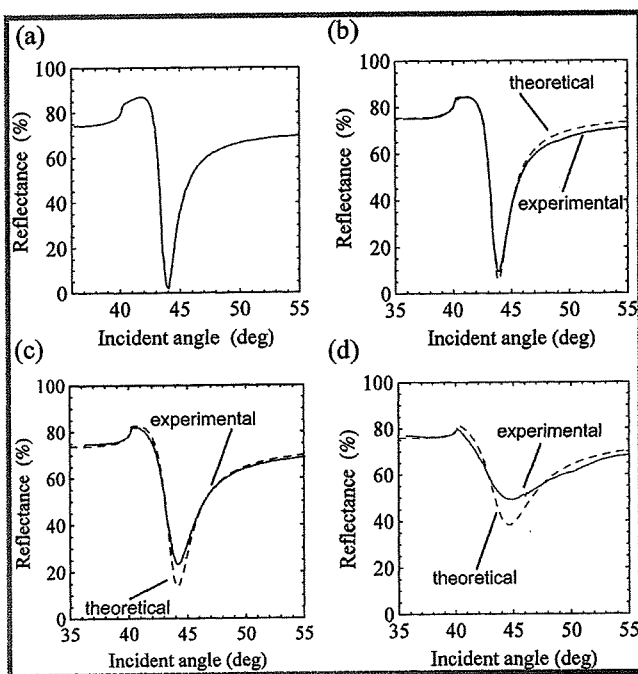

Figure 12. SPR profile measured (solid line) and calculated (broken line) for (a) AUT-covered Au, (b) sample I, (c) sample II, and (d) sample III.
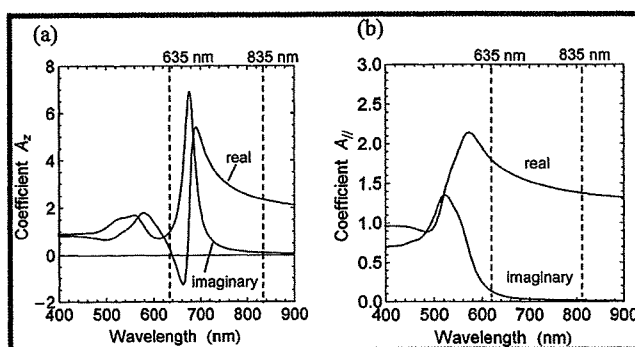
the local field effect should be taken into account for evaluating the dielectric constant ($0.08 < \sigma < 0.2$). The ξ values including the retardation effect is given in Figure 4. Although the dipole sum-up operator Ξ depends on the lattice structure, we showed that Ξ for the square lattice can be used without losing generality. We also showed that the Clausius-Mossoti relation does not necessarily hold in the two-dimensionally distributed NP thin film. We performed SPR measurements for the NP films with different coverages and had agreements between the experimental and the calculated profiles. The results show that our formalism is useful for extracting the optical properties of two-dimensionally distributed metallic NP films on a surface and NP-SPR biosensing.

Using the formalism proposed, we found that large NPs mostly give better amplification factors in the NP-SPR biosensing upon adsorption of NPs at $\lambda = 835$ nm. However, if the parameter A_z is at near resonance, large NPs do not always give large amplification. Careful choice based on the formalism presented in this paper is necessary.

Finally we propose a recipe to evaluate the number of NPs in the NP-SPR biosensing. (i) When the gap distance is unknown, one should measure the red-shifted LSP peak wavelength by absorption spectroscopy.[39] The gap distance with respect to the peak wavelength is found in Figure 3. (ii) Evaluate the A_z and $A_{//}$ values using Figure 2, in which the A_q values are shown as a function of the wavelength or R/d. (iii) Estimate the appropriate value of σ. We can fit the theoretical SPR curve to the experimentally obtained one using the dielectric constant of the NP film, ε_{NP} given by eq 29, using the transfer matrix method. Since the parameter A is given by calculation, only a fitting parameter is σ.

Supporting Information Available: Figure 1S: Comparison of SPR profiles between measured and calculated by the effective medium approximation. Figure 2S: The parameter A_z and $A_{//}$ in water. Figure 3S: The dielectric constants calculated by a linear combination and EMA. Figure 4S: Calculated SPR profiles for different wavelength and different ambient medium. Figure 5S: Calculated SPR profiles taking into account the contribution of the substrate for different size of NPs. This material is available free of charge via the Internet at http://pubs.acs.org.

References and Notes

(1) Bohren, C. F.; Huffman, D. R. *Absorption and Scattering of Light by Small Particles*; Wiley: NewYork, 1983.

(2) Kawata, S., Ed.; *Near-Field Optics and Surface Plasmon Polaritons*; Springer: Berlin, 2001.

(3) Meriaudeau, F.; Downey, T. R.; Passian, A.; Wig, A.; Ferrell, T. L. *Appl. Opt.* **1998**, *37*, 8030.

(4) Okamoto, T.; Yamaguchi, I.; Kobayashi, T. *Opt. Lett.* **2000**, *25*, 372.

(5) Okamoto, T.; Yamaguchi, I. *J. Phys. Chem. B* **2003**, *107*, 10321.

(6) Kume, T.; Hayashi, S.; Yamamoto, K. *Phys. Rev. B* **1997**, *55*, 4774.

(7) Abe, S.; Kajikawa, K. *Phys. Rev. B* **2006**, *74*, 035416.

(8) Tsuboi, K.; Abe, S.; Fukuba, S.; Shimojo, M.; Tanaka, M.; Furuya, K.; Fujita, K.; Kajikawa, K. *J. Chem. Phys.* **2006**, *125*, 174703.

(9) Tsuboi, K.; Fukuba, S.; Naraoka, R.; Fujita, K.; Kajikawa, K. *Appl. Opt.* **2007**, *46*, 4486.

(10) Gupta, G.; Tanaka, D.; Ito, Y.; Shibata, D.; Shimojo, M.; Fukuya, K.; Mitsui, K.; Kajikawa, K. *Nanotechnology* **2009**, *20*, 25703.

(11) Mitsui, K.; Handa, Y.; Kajikawa, K. *Appl. Phys. Lett.* **2004**, *85*, 4231.

(12) Holland, W. R.; Hall, D. G. *Phys. Rev. Lett.* **1984**, *52*, 1041.

(13) Endo, T.; Yamamura, S.; Nagatani, N.; Morita, Y.; Takamura, Y.; Tamiya, E. *Sci. Tech. Adv. Mater.* **2005**, *6*, 491.

(14) Nath, N.; Chilkoti, A. *Anal. Chem.* **2002**, *74*, 504.

(15) Nath, N.; Chilkoti, A. *Anal. Chem.* **2004**, *76*, 5370–5378.

(16) Ghosh, S. K.; Pal, T. *Chem. Rev.* **2007**, *107*, 4797.

(17) Homola, J. *Chem. Rev.* **2008**, *108*, 462.

(18) Fan, X.; White, I. M.; Shopova, S. I.; Zhu, H.; Suter, J. D.; Sun, Y. *Anal. Chim. Acta* **2008**, *620*, 8.

(19) Xu, H.; Käll, M. *Sens. Actuators B* **2002**, *87*, 244.

(20) Hutter, E.; Fendler, J. H.; Roy, D. *J. Phys. Chem. B* **2001**, *105*, 11159.

(21) Lyon, L. A.; Musick, M. D.; Natan, M. J. *Anal. Chem.* **1998**, *70*, 5177.

(22) Lyon, L. A.; Pena, D. J.; Natan, M. J. *J. Phys. Chem. B* **1999**, *103*, 5826.

(23) Hutter, E.; Pileni, M.-P. *J. Phys. Chem. B* **2002**, *107*, 6497.

(24) Ito, M.; Nakamura, F.; Baba, A.; Tamada, K.; Ushijima, H.; Lau, K. H. A.; Manna, A.; Knoll, W. *J. Phys. Chem. C* **2007**, *111*, 11653.

(25) Nakamura. F.; Ito. M.; Manna. A.; Tamada, K.; Hara, M.; Knoll, W. *Jpn. J. Appl. Phys.* **2006**, *45*, 1026.

(26) Jen, Y.-J.; F-Chiang, S.-H.; Liu, F.-K. *Jpn. J. Appl. Phys.* **2006**, *45*, 1850.

(27) He, L.; Smith, E. A.; Natan, M. J.; Keating, C. D. *J. Phys. Chem. B* **2004**, *108*, 10973.

(28) Chen, S.-J.; Chien, F. C.; Lin, G. Y.; Lee, K. C. *Opt. Lett.* **2004**, *29*, 1390.

(29) Wu, B.; Wang, Q. *Chin. Opt. Lett.* **2008**, *6*, 323.

(30) Rueda, A.; Stemmler, M.; Bauer, R.; Fogel, Y.; Mullen, K.; Kreiter, M. *J. Phys. Chem. C* **2008**, *12*, 14801.

(31) Yamaguchi, T.; Yoshida, S.; Kinbara, A. *J. Opt. Soc. Am.* **1974**, *64*, 1563.

(32) Carlan, A.; Desrousseaux, G. *J. Opt. Soc. Am.* **1978**, *68*, 1019.

(33) Yamaguchi, T.; Takahashi, H.; Sudoh, A. *J. Opt. Soc. Am.* **1978**, *68*, 1039.

(34) Yamaguchi, T.; Yoshida, S.; Kinbara, A. *Thin Solid Films* **1973**, *18*, 63.

(35) Yamaguchi, T.; Yoshida, S.; Kinbara, A. *Thin Solid Films* **1974**, *21*, 173.

(36) Aravind, P. K.; Metiu, H. *Surf. Sci.* **1983**, *124*, 506.

(37) Ruppin, R. *Surf. Sci.* **1983**, *127*, 108.

(38) Wind, M. M.; Vlieger, J.; Bedeaux, D. *Physica A* **1987**, *141*, 33.

(39) Uchiho, Y.; Kajikawa, K. *Chem. Phys. Lett.* **2009**, *478*, 211.

(40) Johnson, P. B.; Christy, R. W. *Phys. Rev. B* **1972**, *6*, 4370.

(41) Bagchi, A.; Barrera, R. G.; Fuchs, R. *Phys. Rev. B* **1982**, *25*, 7086.

(42) Bagchi, A.; Barrera, R. G. *Phys. Rev. Lett.* **1980**, *44*, 1475.

(43) Ui, H.; Tomioka, A.; Nishiwaki, T.; Miyano, K. *J. Chem. Phys.* **1994**, *101*, 6430.

(44) Topping, J. *Proc. Soc. Ser. A London* **1927**, *114*, 67.

(45) Bethune, D. S. *J. Opt. Soc. Am. B* **1989**, *6*, 910.
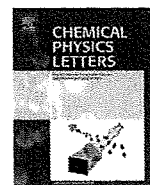
Evaluation of gap distance between gold nanospheres and a gold substrate by absorption spectroscopy

Yuichi Uchiho, Kotaro Kajikawa *

Interdisciplinary Graduate School of Science and Engineering, Tokyo Institute of Technology, Nagatsuta, Midori-ku, Yokohama 226-8502, Japan

ARTICLE INFO

ABSTRACT

An analytical formalism is proposed to calculate polarizability of surface immobilized gold nanospheres (SIGNs) above a gold surface. Using this formalism, we can evaluate the gap distance and its distribution in the SIGN system under various conditions. Experimental results show that the gap distance is much smaller than the thickness of the gap-supporting layer with no adsorbed gold nanospheres. This means that the layer under the nanosphere is collapsed or disordered, stemming from the existence of the SIGNs.

© 2009 Elsevier B.V. All rights reserved.

A large number of studies have appeared on localized surface plasmons (LSPs) in metallic nanoparticles [1–5]. Surface immobilized gold nanospheres (SIGNs) supported by a surfactant layer on a metallic substrate are one of the most promising systems for excitation of LSPs. The SIGNs form by a simple process such that a surfactant-modified metallic substrate is immersed in a gold nanosphere solution. Redshifted absorption peaks with respect to the LSP band of isolated nanospheres are observed for p-polarized light, as a result of electromagnetic interaction between the gold nanospheres and the metallic substrate [6–8]. This interaction yields considerably enhanced electric fields adjacent to the nanospheres at the resonance condition of LSP. This effect can be applied to nonlinear optical phenomena [8,9] and surface enhanced Raman scattering spectroscopy [10].

For reliable analysis of the optical response, an analytical formalism to describe the polarizability of the SIGN systems is necessary. Wind et al. [11] previously reported an analytical formalism to evaluate the polarizability of nanospheres located above a substrate, and a number of calculations have been carried out, on the basis of their formalism [6,8,9,12]. However, the Wind's formalism does not include the dielectric constant of the gap-supporting layer. Hence the previous studies take into account the contribution of the gap-supporting layer using an effective ambient dielectric constant that gives the observed peak wavelengths, assuming that the gap distance is the same as the thickness of the gap-supporting layer with no gold nanosphere adsorption [6,8,9]. Although the peak wavelength can be reproduced by this method, the calculated polarizability is inconsistent. This is because the polarizability is written in proportional to the ambient dielectric constant as described later.

In this Letter, we propose a manner that takes into account the contribution of the gap-supporting layer, and calculated the absorption spectra of the SIGN systems. The proposed formalism allows us to evaluate the actual gap distance between the nanosphere and the substrate. It was found that the gap distance was smaller than the thickness of the gap-supporting layer without any adsorbed gold nanospheres and was found that the distribution of the gap distance is large (20–30%). We infer that the layer structure will be disordered or collapsed, stemming from adsorption of the nanospheres.

We consider a SIGN system illustrated in Fig. 1a, consisting of an ambient medium (relative dielectric constant ε_1), a gold substrate (relative dielectric constant ε_2), and a gold nanosphere (radius R and relative dielectric constant ε_3) supported by a thin dielectric layer thickness d with a dielectric constant ε_4. The dielectric constants ε_2 and ε_3 are generally frequency dependent [13], whereas the dispersion of ε_1 is negligible.

Polarizability of a nanosphere, α_q, is generally described as

$$\alpha_q = 4\pi\varepsilon_1 R^3 A_q \quad (q = z \text{ or} //), \tag{1}$$

where $//$ denotes in-plane components, namely x and y. When the nanospheres are regarded as isolated, A_q is isotropic and is simply written as

$$A_q = -\frac{\varepsilon_1 - \varepsilon_3}{2\varepsilon_1 + \varepsilon_3}. \tag{2}$$

When the nanospheres are close to the substrate, the interaction between the nanosphere and the substrate cannot be neglected. Hence we should consider the multipoles to calculate the parameter A_q. The problem to evaluate the parameter A_q was previously solved by Wind et al. [11] when the gap-supporting layer is ignored ($\varepsilon_4 = \varepsilon_1$). Here we slightly develop their formalism to take into account the contribution from the gap-supporting layer. The jth order multipolar coefficients A_{qi} are calculated by the following equations [6,11]:

* Corresponding author. Fax: +81 45 924 5596.
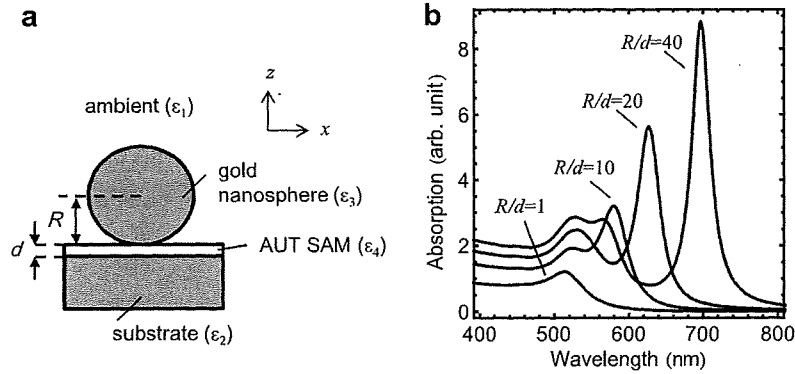E-mail address: kajikawa@ep.titech.ac.jp (K. Kajikawa).

a

b

Fig. 1. (a) The schematic configuration of the SIGN system for calculation. (b) The calculated results of the absorption spectra for different R/d at $\theta = 60°$.

$$\sum_{j=1}^{\infty} \left\{ \delta_{ij} + \frac{k(k+j)!(\varepsilon_2 - \varepsilon_1)(\varepsilon_1 - \varepsilon_3)}{(\varepsilon_1 + \varepsilon_2)((k+1)\varepsilon_1 + k\varepsilon_3)k!j!(2r_z)^{k+j+1}} \right\} A_{\perp j}$$

$$= \frac{\varepsilon_3 - \varepsilon_1}{2\varepsilon_1 + \varepsilon_3} \delta_{k1} \quad (k = 1,2,3,\ldots) \tag{3}$$

$$\sum_{j=1}^{\infty} \left\{ \delta_{ij} + \frac{k(k+j)!(\varepsilon_2 - \varepsilon_1)(\varepsilon_1 - \varepsilon_3)}{(\varepsilon_1 + \varepsilon_2)((k+1)\varepsilon_1 + k\varepsilon_3)(k+1)!(j-1)!(2r_\parallel)^{k+j+1}} \right\} A_{\parallel j}$$

$$= \frac{\varepsilon_3 - \varepsilon_1}{2\varepsilon_1 + \varepsilon_3} \delta_{k1} \quad (k = 1,2,3\ldots) \tag{4}$$

where δ_{kj} is Kronecker's delta. In order to take into account the contribution of the gap-supporting layer, r_z and $r_\parallel$ are defined as;

$$r_z = 1 + \frac{\varepsilon_1}{\varepsilon_4}\frac{R}{d}, \tag{5a}$$

$$r_\parallel = 1 + \frac{R}{d}. \tag{5b}$$

The existence of the gap layer reduces the effective gap distance by a factor of $\varepsilon_4/\varepsilon_1$ for the electric fields normal to the surface, because of the continuity of electric flux across the boundary. The first order coefficient A_{q1} is responsible for the polarizability of nanospheres, i.e., $A_q = -A_{q1}$. Absorption Q in the transmission direction for p-polarized light is described as [6]:

$$Q \propto \frac{\sqrt{(\sin\theta \mathrm{Im}[\alpha_z])^2 + (\cos\theta \mathrm{Im}[\alpha_\parallel])^2}}{\lambda}, \tag{6}$$

where λ and θ are the wavelength and the angle of incidence, respectively. Fig. 1b shows the typical absorption spectra of the SIGN supported by a dielectric film ($\varepsilon_4 = 2.25$), calculated at $R/d = 1, 10, 20, 40$ in air. The calculation was made at $\theta = 60°$. There are two peaks in the spectra: one the LSP band at about 520 nm (band A) and the other a redshifted LSP band (band B), arising from the interaction between the nanosphere and the substrate. Band A is scarcely shifted with the ratio R/d or the ambient dielectric constant. It is reported by numerical calculation that band A is due to surface plasmons propagating along the gold surface [14]. In contrast, the amount of redshift of the band B increases with the ratio R/d, as a result of an increase in the interaction. The solid line in Fig. 2 shows the calculated peak wavelengths of band B as a function of the ratio R/d ($\varepsilon_4 = 2.25$). Similar relation was shown in previous papers [6,9], where the contribution of the gap layer was ignored [12] or was taken into account using the effective ambient dielectric constant of 2.0, instead of 1.0 [6,8,9]. This parameterization is somewhat ad hoc and only peak wavelengths can be predicted. Instead, as mentioned above, we use r_z which is an effective gap distance normalized by $\varepsilon_4/\varepsilon_1$ to consider the contribu-
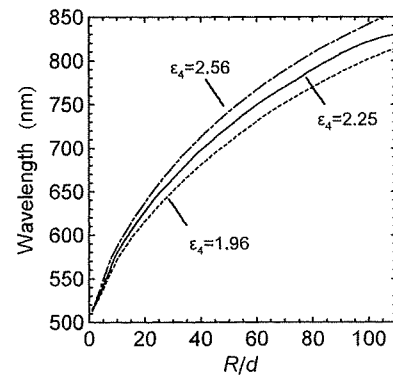
Fig. 2. Peak wavelengths of band B as a function of R/d at $\varepsilon_4 = 1.96, 2.25$ and 2.56.

tion of the gap layer. With this formalism, we can estimate the gap distance, d, since the radius of the gold nanosphere, R, is known.

A 1 nm-thick chromium thin film and a 50 nm-thick gold thin film were deposited on a glass substrate by a vacuum evaporation. The chromium thin film is deposited for promoting adhesion of the gold thin film to the substrate. Aminoundecanethiol (AUT) purchased from Dojindo Laboratory, Japan, was dissolved in ethanol at a concentration of 0.1 mM. The AUT self-assembled monolayer (SAM) was prepared by immersion of the gold substrate in the solution for 2 h followed by rinsing with ethanol. Successively the AUT SAM-covered gold substrate was immersed in an aqueous gold colloidal solution for 50 min to form a gold nanosphere film. The gold nanosphere solutions were purchased from Tanaka Kikinzoku K.K., Japan. Then the substrate was rinsed with pure water.

Transmission absorption spectroscopy was carried out with a MCPD-3000 spectrometer (Otsuka Denshi Ltd., Japan). Light from a halogen lamp was guided by an optical fiber was passed through a polarizer, and was incident to the sample at a 60° incidence with respect to the surface normal. The transmitted light was conveyed to the spectrometer with another optical fiber. The spectra were taken with an accumulation time of 30 ms. The absorption spectra were taken in three different ambient media, (air ($\varepsilon_1 = 1$), water ($\varepsilon_1 = 1.769$) and glycerol ($\varepsilon_1 = 2.161$)).

Fig. 3 shows the p-polarized absorption spectra taken in different ambient media (solid line). Each spectrum has both band A and band B. They are deconvoluted and are plotted with dashed line. The peak wavelengths and the full width at half maximum (FWHM) values are listed in Table 1. The origin of the band at 450 nm observed in spectrum Fig. 3c (glycerol ambient) is unknown, so far. A possible reason is contribution of higher order multipoles such as quadrupole, which was previously predicted
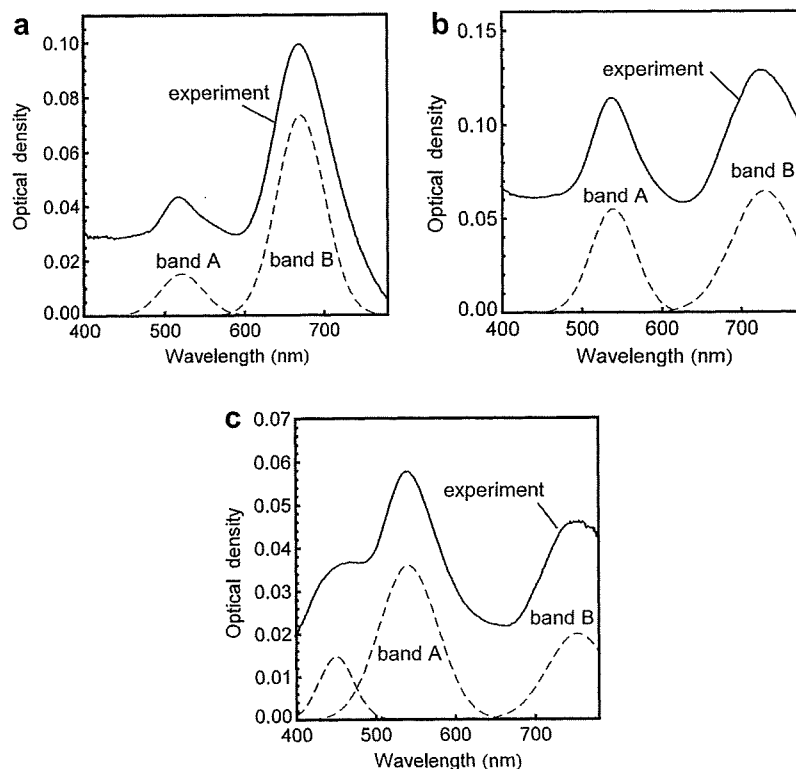
Fig. 3. Absorption spectra experimentally obtained (solid line) and their deconvoluted curves (dashed line) in an ambient medium of (a) air, (b) water, and (c) glycerol.

Table 1
The observed peak wavelengths and the evaluated values of the center value and the standard deviation of the gap distance, d, for different ambient media.

	Observed		Evaluated	
	Peak wavelength (nm)	FWHM (10^{15} Hz)	d_0 (nm)	σ_d (nm)
Air	670.3	0.030	0.75	0.21
Water	729.5	0.038	0.70	0.30
Glycerol	753.1	0.048	0.67	0.30

[15]. The blueshifted band due to quadrupoles is not nevertheless found in the multipole spectra calculated using Eqs. (2) and (3), so far. Further studies are necessary to find the origin of band C. Band B is absent for s-polarized illumination. This indicates that the band B is attributed to the surface normal component, A_z. The amount of redshift of band B increases with ε_1, whereas band A is scarcely shifted. The band B in each spectrum is broader than the corresponding band in the calculated spectra shown in Fig. 1b. The possible reasons are distribution of the gap distance, d, and the size of the gold nanosphere, R. To evaluate the distribution, we used the normal distribution function with respect to x, $G(x, \mu, \sigma)$, where μ and σ denote the center value and the standard deviation. The mean polarizability $\langle \alpha_q \rangle$ was calculated taking into account the distribution of d and R with the formula

$$\langle \alpha_q \rangle = 4\pi \varepsilon_1 R_0^3 \int \int A_q G(d, d_0, \sigma_d) G(R, R_0, \sigma_r) \quad d(R)d(d). \tag{7}$$

The spectra were calculated with $\langle \alpha_q \rangle$ to consider the distribution of d and R, in which dielectric constant $\varepsilon_4 = 2.25$ was used. The center value of the nanosphere $R_0 = 25$ nm and the standard deviation $\sigma_R = 1.9$ nm were used, according to the datasheet. The center value of the gap-supporting layer, d_0, was determined with the peak

wavelength using the relation in Fig. 2. The standard deviation of the gap distance, σ_d, was determined to give the same FWHM as the FWHM of the experimental spectra (band B in Fig. 3). These values are listed in Table 1. The evaluated gap distance d_0 is much smaller than the thickness of the AUT SAM without any gold nanospheres (1.4 nm) [16,17]. The adsorption of gold nanosphere may cause collapse or disordering of the AUT SAM below the nanospheres. In addition, we made the absorption spectroscopy for the SIGNs with different R values and evaluated the gap distances. They are summarized in Fig. 4. A clear tendency is found that the gap distance decreases with the size of the gold nanosphere. This result suggests that the molecules in a nanostructure are not necessarily in the same fashion as they are in SAMs without any perturbation, such as adsorption of nanospheres.
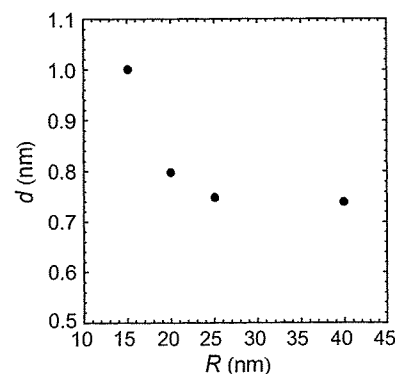

Fig. 4. Central value of the gap distance, d_0, with respect to sizes of gold nanospheres, R.

Finally we consider the dependence of d/R on ε_4. The permittivity ε_4 of the gap-supporting layer may deviate from that of the AUT SAM in the absence of nanospheres when it is collapsed or disordered. Fig. 2 shows the plots of d/R at different ε_4 values ($\varepsilon_4 = 1.96$, 2.25 and 2.56). One may see that the difference in d/R is small: a ca. 13% increase in the permittivity results in a 0.1 nm increase in d for nanospheres of $R = 25$ nm. It is likely that the change in the permittivity due to the collapse or the disordering is within the degree of the standard deviation σ_d.

In summary, we proposed a manner to predict the optical response of SIGNs, taking into account the contribution of the gap-supporting layer. This formalism allows us to evaluate the gap distance between the nanosphere and the substrate. The experimental results show the gap distance of AUT SAMs much smaller than the thickness of AUT SAMs with no adsorbed nanospheres. We infer that adsorption of the gold nanosphere brings about local collapse or disordering of the gap-supporting layer under the nanosphere.

References

[1] A.J. Haes, R.P. Van Duyne, J. Am. Chem. Soc. 124 (2002) 10596.
[2] T. Okamoto, I. Yamaguchi, T. Kobayashi, Opt. Lett. 25 (2000) 372.
[3] N. Nath, A. Chilkoti, Anal. Chem. 76 (18) (2004) 5370.
[4] L.A. Lyon, M.D. Musick, M.J. Natan, Anal. Chem. 70 (1998) 5177.
[5] S. Lal, S. Link, N.J. Halas, Nat. Photon. 1 (2007) 641.
[6] T. Okamoto, I. Yamaguchi, J. Phys. Chem. B 107 (2003) 10321.
[7] T. Kume, S. Hayashi, K. Yamamoto, Phys. Rev. B 55 (1997) 4774.
[8] S. Abe, K. Kajikawa, Phys. Rev. B 74 (2006) 035416.
[9] K. Tsuboi et al., J. Chem. Phys. 125 (2006) 174703.
[10] J. Wang, T. Zhu, M. Tang, S.M. Cai, Z.F. Liu, Jpn. J. Appl. Phys. 35 (1996) 1381.
[11] M.M. Wind, J. Vlieger, D. Bedeaux, Physica A 141 (1987) 33.
[12] A. Rueda, M. Stemmler, R. Bauer, Y. Fogel, K. Mullen, M. Kreiter, J. Phys. Chem. C 112 (2008) 14801.
[13] P.B. Johnson, R.W. Christy, Phys. Rev. B 6 (1972) 4370.
[14] G. Leveque, O.J.F. Martin, Opt. Exp. 14 (2006) 9971.
[15] P. Nordlander, E. Prodan, Nano Lett. 4 (2004) 2209.
[16] M. Watanabe, K. Kajikawa, Sens. Actuators, B 89 (2003) 126.
[17] S. Fukuba, K. Tsuboi, S. Abe, K. Kajikawa, Langmuir 24 (2008) 8367.

Cross-sectional Transmission Electron Microscopy and Optical Characterization of Gold Nanoislands

Gaurav Gupta, Yoshiko Nakayama[1], Kazuo Furuya[1], Kazutaka Mitsuishi[1], Masayuki Shimojo[1,2], and Kotaro Kajikawa*

Interdisciplinary Graduate School of Science and Engineering, Tokyo Institute of Technology, Yokohama 226-8502, Japan
[1] *High Voltage Electron Microscopy Station, National Institute for Materials Science, Tsukuba, Ibaraki 305-0003, Japan*
[2] *Advanced Science Research Laboratory, Saitama Institute of Technology, Fukaya, Saitama 369-0293, Japan*

In this paper, we present the cross-sectional transmission electron microscope images of gold nanoislands formed by annealing ultrathin gold films to correctly determine the nanoisland three-dimensional shapes. The samples studied were 5 and 7 nm gold films deposited on quartz and annealed at 500 and 900 °C. The cross-sectional view of the gold nanoislands confirmed that they appear to be like truncated spheres and not like the usually assumed spheroids. The shape of the nanoislands varied from spherical to hemispherical under different sample fabrication conditions. These shapes are consistent with the results predicted by polarized absorption spectroscopy.
© 2009 The Japan Society of Applied Physics

Gold nanoisland films, prepared by the annealing of ultrathin films, have been studied for many years. The optical properties of such films have been theoretically investigated assuming that they comprise rotational ellipsoids lying along the surface.[1-4] However, they may not be rotational ellipsoids but truncated spheres or partial spheres from the viewpoint of minimum surface energy. Recently, we have reported such shapes of gold nanoislands on the basis of the results of absorption spectroscopy and theoretical calculatitons, in which the degree of truncation of the nanoislands is quantitatively estimated.[5] To correctly determine the shapes of the nanoislands, another probe (imaging probe) other than that of spectroscopy is necessary. The imaging techniques, such as scanning electron microscopy and atomic force microscopy, are unable to reveal the three-dimensional (3D) shapes of the nanoislands. Thus, in this paper, we present the cross-sectional transmission electron microscopy (TEM) measurements to clarify the shapes of gold nanoislands and to validate the applied truncated sphere model.

Ultrathin gold films of 5 and 7 nm thicknesses were deposited on clean and dried quartz substrates. The coated substrates were then annealed in a furnace at 500 and 900 °C for 2 h with a rise time of 30 min. For the fabricated samples, transmission absorption spectroscopic measurements were conducted with incident E-field parallel to the substrate (s-polarized light). Later, the cross-sectional TEM measurements were conducted for the fabricated samples. The samples were coated with carbon to protect the gold films and sectioned using a focused ion beam. The sectioned samples were picked up and glued onto TEM grids. Then, they were observed using a transmission electron microscope (JEOL JEM-3000F) in bright field and high-resolution modes.

Figure 1 shows a plot of the calculated peak absorption wavelength for E-field parallel to the substrate as a function of the shape angle (θ_{sh}) of the truncated gold island (shown in the inset of Fig. 1).[5] The peak wavelength blueshifts from 568.3 to 510.9 nm as θ_{sh} varies from 90° (hemisphere) to 180° (sphere). Since the size of the particles is much smaller
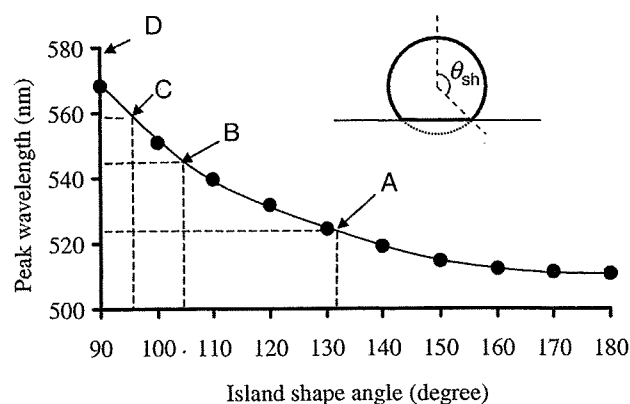
*E-mail address: kajikawa@ep.titech.ac.jp

Fig. 1. Plot of calculated peak absorption wavelength as a function of shape angle of gold nanoisland on a quartz substrate.

Table I. Measured peak absorption wavelengths and estimated shape angles for four fabricated samples.

| Sample	Thickness (nm)	Annealing temp. (°C)	Peak (nm)	θ_{sh} (°)
A	5	900	523.1	~132
B	5	500	545.9	~105
C	7	500	559.1	~95
D	7	500	579.3	<90

than the wavelength of light, the optical retardation effect is negligibly small and the quasi-static approximation holds. Hence, the peak wavelength is independent of the size of the particles. Table I shows the fabrication details of four gold nanoisland film samples considered for the measurements along with their measured peak absorption wavelengths and average θ_{sh} values. The average θ_{sh} values were obtained from Fig. 1 against the corresponding value of the measured peak absorption wavelength. Note that samples C and D have the same gold film thickness and annealing temperature. Since their peak wavelengths were different owing to their different gold nanoisland shapes, both were considered separately for the cross-sectional TEM measurements.
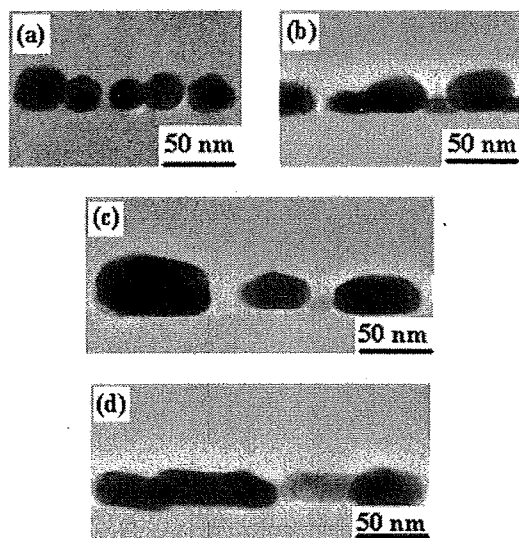
Fig. 2. Cross-sectional TEM images. (a) Sample A: 5 nm gold film annealed at 900 °C; (b) sample B: 5 nm gold film annealed at 500 °C; (c) sample C: 7 nm gold film annealed at 500 °C; (d) sample D: 7 nm gold film annealed at 500 °C.

Figure 2 shows the measured cross-sectional TEM images for the four samples listed in Table I. The islands appear to be like truncated spheres. No damage due to the focused ion beam was observed over the image area. The degree of truncation increases in the order of samples A < B < C < D. Clearly, islands in sample A [Fig. 2(a)] are more spherical and those in sample C [Fig. 2(c)] are almost hemispherical. For sample D [Fig. 2(d)], the islands appear flatter than hemispheres. Samples C and D were fabricated under the same conditions but have different island shapes and hence different peak absorption wavelengths. This was due to the poor reproducibility of samples prepared with thicker gold films (7 nm). Figure 3 shows the magnified images of individual islands for samples A–C. These images are in fair agreement with the corresponding predicted shape angle listed in Table I for each sample. This justifies the applicability of the theoretical model of truncated spheres.
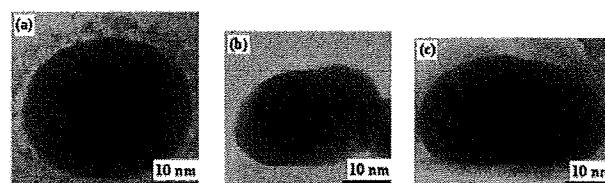
Fig. 3. Magnified cross-sectional TEM images. (a) Sample A: 5 nm gold film annealed at 900 °C; (b) sample B: 5 nm gold film annealed at 500 °C; (c) sample C: 7 nm gold film annealed at 500 °C.

Also, the cross-sectional TEM images indicate that the shape of a gold nanoisland is more truncated for a thicker gold film and less truncated at a higher annealing temperature. This result supports the conclusions drawn from our quantitative structure estimation of gold nanoislands, using polarized absorption spectroscopy.[5]

In summary, the cross-sectional TEM images revealed the true shapes of gold nanoislands formed by annealing ultrathin gold films. The nanoislands appeared to be like truncated spheres with various degrees of truncation, not spheroids with different aspect ratios. The degree of truncation was higher for thicker gold films and lower at higher annealing temperatures. Figure 3(c) shows that nearly hemispherical islands are obtainable. The shapes of such islands are consistent with the results predicted by polarized absorption spectroscopy.[5]

1) S. W. Kennerly, J. W. Little, R. J. Warmack, and T. L. Ferrell: Phys. Rev. B **29** (1984) 2926.
2) R. Chauvaux and A. Meessen: Thin Solid Films **62** (1979) 125.
3) R. J. Warmack and S. L. Humphrey: Phys. Rev. B **34** (1986) 2246.
4) F. Hubenthal, C. Hendrich, H. Ouacha, D. Blázquez-Sánchez, and F. Träger: Int. J. Mod. Phys. B **19** (2005) 2604.
5) G. Gupta, D. Tanaka, Y. Ito, D. Shibata, M. Shimojo, K. Furuya, K. Mitsui, and K. Kajikawa: Nanotechnology **20** (2009) 025703.

Short Communication

Identification of a novel biomarker for oxidative stress induced by hydrogen peroxide in primary human hepatocytes using the 2-nitrobenzenesulfenyl chloride isotope labeling method

Yoichiro Takami,[1,2] Hirofumi Uto,[1] Tsutomu Tamai,[1] Yuko Sato,[2] Yo-ichi Ishida,[2] Hiroyuki Morinaga,[3] Yoichi Sakakibara,[2,4] Akihiro Moriuchi,[1] Makoto Oketani,[1] Akio Ido,[1] Tomoaki Nakajima,[5] Takeshi Okanoue[6] and Hirohito Tsubouchi[1]

[1]Department of Digestive and Lifestyle-related Disease, Health Research, Human and Environmental Sciences, Kagoshima University Graduate School of Medical and Dental Sciences, Kagoshima, [2]Miyazaki Prefectural Industrial Support Foundation, [3]Research Institute, Unkai Shuzo, [4]Department of Biochemistry and Applied Biosciences, Faculty of Agriculture, University of Miyazaki, Miyazaki, [5]Molecular Gastroenterology and Hepatology, Graduate School of Medical Science, Kyoto Prefectural University of Medicine, Kyoto and, [6]Department of Hepatology, Saiseikai Suita Hospital, Osaka, Japan

Aim: Oxidative stress is involved in the progression of non-alcoholic steatohepatitis (NASH). However, there are few biomarkers that are easily measured and accurately reflect the disease states. The aim of this study was to identify novel oxidative stress markers using the 2-nitrobenzenesulfenyl (NBS) stable isotope labeling method and to examine the clinical utility of these diagnostic markers for NASH.

Methods: Proteins extracted from phosphate buffered saline- and hydrogen peroxide-loaded human primary hepatocyte were labeled with the [^{12}C]- and [^{13}C]-NBS reagents, respectively. Pairs of peaks with 6-Da differences in which the [^{13}C]-NBS labeling was more intense than the [^{12}C]-NBS labeling were detected by MALDI-TOF/MS and identified by MS/MS ion searching.

Results: Four pairs of peaks, m/z 1705–1711, m/z 1783–1789, m/z 1902–1908 and m/z 2790–2796, were identified as

cytochrome c oxidase VIb (COX6B), liver carboxylesterase 1 (CES1), carbamoyl-phosphate synthase 1 (CPS1) and superoxide dismutase (MnSOD), respectively. Furthermore, serum MnSOD protein levels were significantly higher in NASH patients than in simple steatosis (SS) patients. The serum MnSOD levels tended to increase in parallel with the stage of fibrosis.

Conclusion: The NBS labeling technique was useful to identify biomarkers. Serum MnSOD may be a useful biomarker that can distinguish between SS and NASH.

Key words: 2-nitrobenzenesulfenyl, oxidative stress, MnSOD, non-alcoholic steatohepatitis

INTRODUCTION

IN SEVERAL LIVER diseases, including non-alcoholic steatohepatitis (NASH) and chronic hepatitis C (CHC), oxidative stress is a major pathogenetic event.

Lipid peroxidation, free radical generation, CYP2E1 induction and mitochondrial dysfunction are known to induce oxidative stress and contribute to the progression of NASH and CHC.[1–3] Therefore, oxidative stress markers should be biomarkers that reflect the pattern and strength of oxidative stress and disease progression. Several oxidative stress markers for liver diseases including 8-hydroxy-2′-deoxyguanosine (8-OHdG), superoxide dismutase (SOD) and thioredoxin are well known. However, the clinical significance of these markers has not been fully evaluated.[4–6] Thus, oxidative stress markers that accurately reflect disease states and